jove

Identification and Quantification of Decomposition Mechanisms in Lithium-Ion Batteries; Input to Heat Flow Simulation for Modeling Thermal Runaway

Ibtissam Adanouj[1], **Ákos Kriston**[2], **Vanesa Ruiz**[1], **Andreas Pfrang**[1]

[1] European Commission, Joint Research Centre (JRC), The Netherlands [2] European Commission, Joint Research Centre (JRC), Italy

Corresponding Author

Ibtissam Adanouj
ibtissam.adanouj@ec.europa.eu

Citation

Adanouj, I., Kriston, Á., Ruiz, V., Pfrang, A. Identification and Quantification of Decomposition Mechanisms in Lithium-Ion Batteries; Input to Heat Flow Simulation for Modeling Thermal Runaway. *J. Vis. Exp.* (181), e62376, doi:10.3791/62376 (2022).

Date Published

March 7, 2022

DOI

10.3791/62376

URL

jove.com/video/62376

Abstract

The risks and possible accidents related to the normal use of lithium-ion batteries remain a serious concern. In order to get a better understanding of thermal runaway (TR), the exothermic decomposition reactions in anode and cathode were studied, using a Simultaneous Thermal Analysis (STA)/Gas Chromatography-Mass Spectrometry (GC-MS)/Fourier Transform Infrared (FTIR) spectrometer system. These techniques allowed the identification of the reaction mechanisms in each electrode, owing to the analysis of evolved gaseous species, the amount of heat released and mass loss. These results provided insight into the thermal events happening within a broader temperature range than covered in previously published models. This allowed the formulation of an improved thermal model to depict TR. The heat of reaction, activation energy, and frequency factor (thermal triplets) for each major exothermic process at material level were investigated in a Lithium Nickel-Manganese-Cobalt-Oxide (NMC (111))-Graphite battery cell. The results were analyzed, and their kinetics were derived. These data can be used to successfully simulate the experimental heat flow.

Introduction

The need of decarbonizing the economy combined with increasing energy demands ─ resulting from socio-economic developments and from climate change ─ requires a major shift in the energy system to address challenges posed by global warming and fuel shortage[1,2]. Clean energy technologies such as wind energy and solar energy are regarded as best alternatives to a fossil-fuel dominated energy system[3]; however, they are intermittent and the storage of energy will help to ensure continuity of energy supply. Properties such as high specific energy density, stable cycling performance and efficiency make lithium-ion batteries (LIBs) promising candidates as electrochemical energy storage system. The cost and the lack of reliable operation of LIBs may hamper a wider application in the

power grid, in the form of large stationary battery system[4,5]. An additional aspect to consider is that the combination of high energetic materials with flammable organic solvent-based electrolytes can lead to hazardous conditions such as fire, release of toxic gases and explosion[6,7]. Therefore, one must address safety issues in LIBs.

Since early commercialization, a number of accidents in current applications (portable electronic devices, electric cars, and auxiliary power unit in aircraft) were reported in the news[8,9]. For instance, despite high quality production, the Sony laptop batteries incident[10], the two Boeing 787 incidents[11,12], Samsung Galaxy Notes 7 incidents[13] are assumed to happen by internal short circuits in a cell. Tests have been developed to assess safety hazards[14,15,16,17]. Overcharge, over-discharge, external heating, mechanical abuse and internal/external short-circuit are failure mechanisms that are known to trigger thermal runaway (TR)[18] and have been included in some standards and regulations. During this process, a series of exothermic reactions occur causing a drastic and rapid increase in temperature. When the heat generated cannot be dissipated fast enough, this condition develops into a TR[19,20]. Additionally, a single cell can then generate sufficient heat to trigger the neighboring cells, within a module or within a pack assembly, into TR; creating a thermal propagation (TP) event. Mitigation strategies such as increasing cell spacing in a module, the use of insulation materials and a specific style of cell interconnecting tab have all proven to curb the propagation phenomenon[21]. Also, the electrolyte stability and the structure stability of various cathode materials in the presence of electrolyte, at elevated temperature, have been investigated in order to reduce the likelihood of TR[22].

Juarez-Robles et al. showed the combined effects of the degradation mechanisms from long-term cycling and over-discharge on LIB cells[23]. Depending on the severity of the discharge, phenomena like Li plating, cathode particle cracking, dissolution of Cu current collector, cathode particle disintegration, formation of Cu and Li bridges were reported as the main degradation mechanisms observed in these tests. Furthermore, they studied the combined effect resulting from aging and overcharge on a LIB cell to shed light on the degradation mechanisms[24]. Due to the extent of the overcharge regime, degradation behaviors observed for the cell were capacity fade, electrolyte decomposition, Li plating, delamination of active material, particle cracking and production of gases. These combined abuse conditions may cause the active materials to undergo exothermic reactions that can generate sufficient heat to initiate thermal runaway.

To avoid safety-related problems, lithium-ion batteries have to pass several tests defined in various standards and regulations[14]. However, variety in cell designs (pouch, prismatic, cylindrical), applicability of tests limited to a certain level (cell, module, pack), different evaluation and acceptance criteria defined, highlight the need to unify guidelines and safety requirements in standards and regulations[25,26,27]. A reliable, reproducible and controllable methodology, with uniform test conditions to trigger an internal short circuit (ISC) with subsequent TR, along with uniform evaluation criteria, is still under development[28]. Furthermore, there is not a single agreed protocol to assess the risks associated with the occurrence of TP in a battery during normal operation[20,25].

In order to establish a testing protocol that simulates a realistic field failure scenario, a massive number of input parameter combinations (e.g., design parameters of the cell such as capacity, surface to volume ratio, thickness of the electrodes,

ISC triggering method, location, etc.) need to be investigated experimentally to determine the best way to trigger TR induced by internal short circuit. This requires prohibitive lab efforts and costs. An alternative approach consists of the use of modeling and simulation to design a suitable triggering method. Nonetheless, 3D-thermal modeling of batteries can be prohibitively computationally expensive, considering the number of assessments needed to cover the effect of all possible combinations of parameters potentially governing TR induced by an internal short circuit.

In the literature, thermal decomposition models have been developed to simulate electrochemical reactions and thermal response of different types of lithium-ion batteries under various abuse conditions, such as nail penetration[29], overcharge[30], or conventional oven test[31]. In an effort to understand the cathode material stability, Parmananda et al. compiled experimental data of accelerating rate calorimeter (ARC) from the literature[32]. They have extracted kinetic parameters from these data, developed a model to simulate the calorimetric experiment and use these kinetic parameters for thermal stability prediction of a range of cathode materials[32].

In references[29,30,31] and numerous other studies, a combination of the same models[33,34,35,36] — describing respectively; heat release from decomposition of anode and solid electrolyte interface (SEI) layer; decomposition of cathode and decomposition of electrolyte — has been used repeatedly during several years as the basis for modeling thermal runaway. The latter has also been improved over time, for instance, by adding venting conditions[37]. However, this series of model was initially developed to capture the onset temperature of a TR and not for modeling thermal runaway severity.

Since thermal runaway is an uncontrolled thermal decomposition of battery components, it is of utmost importance to identify the decomposition reactions in anode and cathode to be able to design safer Li-ion batteries cells and more accurate testing methodologies. To this purpose, the goal of this study is the investigation of thermal decomposition mechanisms in NMC (111) cathode and graphite anode for the development of a simplified yet sufficiently accurate reaction kinetic model, which can be used in simulation of TR.

Here, we propose the use of coupled analytical equipment: Differential Scanning Calorimetry (DSC) and Thermal Gravimetric Analysis (TGA) in a single simultaneous thermal analysis (STA) instrument. This equipment is coupled to the gas analysis system, which consists of Fourier transform infrared spectroscopy (FTIR) and gas chromatography-mass spectrometry (GC-MS). The hyphenated STA/FTIR/GC-MS techniques will allow us to acquire a better understanding of the causes and processes of thermal runaway in a single cell. Moreover, this will help to identify thermal decomposition processes. Hyphenation refers to the online combination of different analytical techniques.

The set-up of this custom-made integrated system is shown in **Figure 1**. The STA equipment, used in the present study, is located inside a glovebox, which guarantees the handling of components in a protective atmosphere. The latter is coupled with the FTIR and GC-MS *via* heated transfer lines (150 °C) to avoid the condensation of evaporated materials along the lines. The hyphenation of these analytical techniques allows simultaneous study of thermal properties and identification of released gases, providing information of the mechanisms of the thermally induced decomposition reactions. In order to further reduce the impact of unwanted chemical reactions in

the electrodes during sample preparation, sample handling and sample loading are performed inside an argon-filled glove box. The disassembled electrodes are not rinsed nor any additional electrolytes are added to the crucible.

STA allows for the identification of phase transitions during the heating process, along with accurate determination of temperatures and enthalpies associated with these phase transitions, including those without mass change. The combination of on-line FTIR and GC-MS methods with the STA provides a qualitative assessment of gases evolved from the sample during its thermal decomposition. This is the key in identifying thermally induced reaction mechanisms. Indeed, STA/FTIR/GC-MS coupled system allows correlating the mass changes, heat flow, and detected gases.

FTIR and GC-MS each have their advantages and limitations. The high sensitivity of GC-MS allows rapid and easy detection of molecules from peaks of low intensity. Furthermore, FTIR data well complement the information provided by MS spectrum patterns to achieve the structural identification of organic volatile species. However, FTIR is less sensitive. In addition, diatomic molecules, such as H_2, N_2, O_2, do not possess a permanent dipole moment and are not infrared active. Therefore, they cannot be detected using infrared absorption. On the contrary, small molecules such as CO_2, CO, NH_3, and H_2O can be identified to a high degree of certainty[38]. Altogether, the information provided by these complementary methods makes it possible to gain insight of the gases emitted during thermal characterization.

In order to check the state of the art in terms of thermal decomposition reactions identified for Lithium Nickel Manganese Cobalt oxide (NMC (111)) cathode, graphite (Gr) anode and 1M $LiPF_6$ in ethylene carbonate (EC)/dimethyl carbonate (DMC) = 50/50 (v/v) electrolyte, a literature review was performed. **Table 1**, **Table 2**, and **Table 3** summarize the main findings.

In the field of thermal characterization of battery components, the sample preparation method has a significant effect on DSC experimental results since this has an influence on the DSC signal. Many studies have reported different approaches in terms of electrode handling. Some variations include 1) scratching active material from electrode without prior rinsing nor adding extra amount of electrolyte, e.g.,[54,55]; 2) rinsing/drying/scratching active material and adding a given amount of electrolyte with it in the crucible e.g.,[55,56]; 3) rinsing/drying/scratching active material without adding electrolyte at a later stage (e.g., see reference[57]). However, in the literature, there is no general agreement on the sample preparation techniques. Washing the electrode affects the integrity and the reactants in the SEI[58], which in turn, modify the amount of heat generated from its decomposition[34,59]. On the other hand, there is no clear indication or sufficient details on the amount of added electrolyte to the harvested materials prior to thermal analysis.

In this work, the SEI modification is minimized by not washing the electrode and excluding electrolyte addition, in an attempt to characterize the electrode material in its original state, while keeping its residual electrolyte content. Realizing that SEI thermal decomposition is a potential trigger to thermal runaway, this preparation method is expected to allow for a better understanding of the thermal properties of the electrode, under test conditions, without the dissolution of some SEI products. Indeed, the breakdown of SEI layer on the anode is generally the first stage of battery failure that initiates a self-heating process[39,41,60].

Another important issue in thermal analysis is the measurement conditions (type of crucible, open/closed

crucible, atmosphere) that are affecting the DSC signal to be measured. In this case, the use of a hermetically closed crucible is clearly not suitable for the hyphenated STA/ GC-MS/FTIR techniques, which implies the identification of evolved gases. In a semi-closed system, the size of the opening in the perforated crucible lid can have a strong influence on the measurement results. If the size is small, the thermal data is comparable to a sealed crucible[61]. On the contrary, a large hole in the lid is expected to decrease the measured thermal signal because of the early release of low temperature decomposition products. As a result, these species would not be involved in higher temperature processes[61]. Indeed, a closed or semi-closed system allows longer residence time of the species, transformed from condensed to vapor phase inside the crucible. A laser-cut vent hole of 5 µm in the crucible lid has been selected for the investigation of thermal behavior and evolved gases of graphite anode and NMC (111) cathode. Considering the size of the laser-cut hole, we assume the system inside the crucible may most probably depict, a simple but reasonable approximation of the dynamic inside both, a closed battery cell and a battery cell venting.

This present work is built upon an earlier publication by the same authors[48]. However, this paper focuses in more detail on the experimental part, highlighting the benefits of the used techniques and testing conditions to reach the goal of this work.

To the best of the authors' knowledge, there is limited research published on the thermal behavior of electrode material, using of the exact combination of these analytical instruments STA/FTIR/GC-MS, analytical parameters and sample preparation/ handling to elucidate chemical reaction mechanisms at material level during thermal decomposition. At the cell level, Fernandes et al. investigated the evolved gases in a continuous way, using FTIR and GC-MS, in a battery cylindrical cell undergoing an overcharged abuse test, in a closed chamber[62]. They have identified and quantified the gases during this test, but the understanding of reaction mechanisms still remains unclear. Furthermore, to develop a TR runaway model, Ren et al. have also conducted DSC experiments at material level to calculate kinetic triplet parameters of exothermic reactions[55]. They have identified six exothermic processes, but the reaction mechanisms were not determined, and they did not use coupled gas analysis techniques.

On the other hand, Feng et al. have proposed a three-stage TR mechanism in LIB cell with three characteristic temperatures that can be used as indexes to assess thermal safety of battery[63]. For this purpose, they have used a thermal database with data from ARC. Nevertheless, details of the chemical reactions underlying these three mechanisms are not provided.

In this study, the data obtained through these thermal analysis methods are essential for the development of the kinetic model where the main thermal decomposition processes should be determined and properly described. The kinetic thermal triplet, namely the activation energy, frequency factor, and heat of reaction, are calculated for the different sub-processes taking place in both electrodes during thermally induced decomposition, using three different heating rates: 5, 10 and 15 °C /min. When applicable, the Kissinger method[64,65] was used for the determination of activation energy and frequency factor, following the Arrhenius equation. The Kissinger method is applicable when DSC peak shifts to higher temperature with increasing heating rate. The reaction enthalpy is obtained by integrating the

area of the reaction peak, as measured by DSC. From these thermal data and the measurement uncertainties, a reaction kinetic model is proposed to simulate the dynamics of a thermal runaway. In the second part of this work[66], this newly developed model will be used to determine the probability of a TR event as a function of the parameters of an ISC triggering method.

The scheme depicted in **Figure 2** summarizes the sequence of steps needed to undertake the protocol. The first step consists of assembling the electrochemical cell with the battery materials under investigation, namely, NMC (111)/Gr.

In order to be able to harvest the battery materials after electrochemical cycling and state of charge (SOC) adjustment to 100%, a re-sealable electrochemical cell supplied by EL-CELL (ECC-PAT-Core) was used. This allowed a smooth cell opening process without damage to the electrodes. Once the battery materials are harvested, thermal characterization is carried out.

Protocol

NOTE: For a detailed explanation of each step, refer to the sub-sections depicted in **Figure 2**.

1. Electrochemical cell preparation procedure inside an argon-filled glove box

1. Insulation sleeve assembly with separator for a 2 or 3-electrode electrochemical cell
    1. Take a polymer separator disc (diameter 22 mm, thickness 25 µm) and place it on the top of the bottom part of the polypropylene insulation sleeve.
    2. Carefully press down the upper part of the insulation sleeve to assemble it. Ensure that the separator is flat.
2. Electrochemical cell assembly

    NOTE: Ensure that all steps related to the electrochemical cell assembly take place inside an argon-filled glove box with O_2 and H_2O < 0.1 ppm.

    1. Gather the necessary tools and materials for this step and insert them inside the glove box: vacuum pick-up tweezers, EL-CELL electrochemical cell (consisting of: stainless steel lower plunger of type 50, stainless steel upper plunger, the assembled insulation sleeve from paragraph 1.1, stainless steel core cell parts), 18 mm graphite disc with rated areal capacity of 2.24 mAh/cm^2, 18 mm NMC (111) disc with rated areal capacity of 2.0 mAh/cm^2, 1.0 M $LiPF_6$ in EC/DMC = 50/50 (v/v), micropipette 100-1,000 µL, micropipette tips.

        NOTE: The specific capacity of graphite and NMC (111) are 350 mAh/g and 145 mAh/g, respectively, and is provided by the manufacturer. Ensure that anode electrode was designed to have a higher capacity than the cathode to avoid Li plating on the graphite anode. Proper balancing of the electrode capacities is of critical importance to avoid overcharging of graphite and Li plating. The areal capacities of electrodes are also provided by the manufacturer.
    2. Weigh the electrode discs on a 4-digit analytical balance and record the values to determine the active material loading (see section 2 Calculation of electrode disc's capacity).

        NOTE: Use production grade graphite anode discs (96% active material, 2% carboxymethyl cellulose (CMC) binder, 2% conductive additive) and NMC (111) cathode discs (86% active material,

8% conductive additive, and 6% Polyvinylidene fluoride binder) to assemble 2 and 3-electrode electrochemical cells (EL-CELL). The assembly in a 2 / 3-electrode electrochemical cell allows reproducing the same Li content in a charged state as in a real large format cell, compared to a Li-metal half-cell assembly. Up to 40 g, the accuracy of the digital balance is of 0.01 mg.

3. Take 150 µL of the electrolyte with the micropipette and put a drop on the separator facing the bottom part of the insulation sleeve. Insert the graphite anode with the help of a vacuum pick-up tweezer followed by the lower plunger.

4. Turn around the insulation sleeve and dispense the remaining electrolyte on the separator. Insert the NMC (111) cathode disc with the help of a vacuum pick-up tweezer and put the upper plunger.

5. Mount the assembly inside the cell core part. Put the O-ring and fasten everything together using the bolt clamp.

6. Measure the nominal voltage of the fresh cell with a multimeter to ensure a good contact between cell components and to identify potential faults. Multimeter voltage resolution is 1 mV at 3 V and 10 mV at 30 V.

   NOTE: To avoid long waiting times after cell opening, which may potentially alter the composition of the active materials, assemble a new 18 mm NMC (111)/Gr electrochemical cell for every thermal experiment. The lead time between the opening of a cell and the STA/evolved gas analysis (including all preparations) should not exceed more than 2 days. Proper assembly and closure of the cell is of utmost importance for successful electrochemical cycling of the cell and hence for the preparation of electrodes for STA/GC-MS/FTIR characterization.

2. Calculation of electrode disc's capacity

NOTE: Bare copper and aluminum foils (non-coated) from the same supplier were cut into discs with a fixed 18 mm diameter.

1. Weigh (at least) 5 Al discs and five Cu discs of 18 mm diameter to calculate the average weight of each current collector.

   1. Prior to each cell assembly, weigh the 18 mm disc NMC electrode and the 18 mm disc Gr anode, as mentioned in step 1.2.2, in order to calculate precisely, at a later stage, the material loading and the calculated areal capacity.

2. Derive the electrode material loading by subtracting the average mass ($W_{non\text{-}coated\ current\ collector}$) of the current collector (non-coated foil) from the electrode disc weight:

   $W_{electrode\ material}\ (mg) = W_{coated\ electrode\ disc}\ (mg) - W_{non\text{-}coated\ current\ collector}\ (mg)$

3. Calculate the active material content:

   $W_{active\ material}$ (mg) = $W_{electrode\ material}$ (mg) * X%

   where X% is the mass fraction of the active material and is provided by the manufacturer (see note after step 1.2.2).

4. Determine the actual capacity of the electrode disc by multiplying the active material content by the rated specific capacity provided by the supplier (see note after step 1.2.1). Afterwards, calculate the areal capacity of the disc:

Calculated capacity electrode disc (mAh) = $W_{active\ material}$ (g) * *Rated specific capacity* (mAh/g)

Calculated areal capacity electrode disc (mAh/cm^2) = *Calculated capacity electrode disc* (mAh) / πr^2

r = radius of the electrode disc

NOTE: Steps 2.1-2.4 are performed to accurately determine the mass loading and the areal capacity of each electrode and verify the reported values by the supplier (i.e., 2.24 mAh/cm^2 for the graphite anode and 2.0 mAh/cm^2 for the NMC (111) cathode).

3. Electrochemical cycling

1. Establish a cycling protocol with the battery cycler software as described by Ruiz et al.[67] under section 1 (Pouch Cell Preparation and Formation), paragraph 3 and the supplementary files of Ruiz et al.[67] manuscript.

   NOTE: The electrochemical cycling performed in section 3 is an initial formation cycle to activate the cell, to measure the capacity and finally to adjust the SOC. Each cell undergoes two charge-discharge cycles and is then fully charged (at the cut-off voltage of 4.2 V). The number of cycles has been selected according to the supplier recommendation.

2. Following the procedure described by Ruiz et al.[67], include the following steps into the electrochemical cycling procedure (see **Supplementary File 1**): constant current (CC) charge at C/20 to cut-off voltage 4.2 V; 1 h rest time (OCV); CC discharge at C/20 to cut-off voltage 3 V; 1 h rest time (OCV); CC charge at C/20 to cut-off voltage 4.2 V; 1 h rest time (OCV); CC discharge at C/20 to cut-off voltage 3 V; 1 h rest time (OCV); CC charge at C/20 to cut-off voltage 4.2 V.

   NOTE: Since the real capacity of the electrochemical cell cannot be determined before the initial formation cycle, the testing current corresponding to a C-rate of C/20 was determined based on the calculated capacity of the electrode disc (see details in step 2.4). As a result, a capacity of 5.18 mAh can be estimated. Since a 1C rate refers to a full charge or discharge of the electrochemical cell in 1 h, a current corresponding to a C/20 rate is therefore calculated as 5.18 mAh / 20 h = 0.259 mA. Therefore, a constant current of 0.259 mA was applied until the corresponding cut-off criteria for charge and discharge.

3. Provide a file name to this protocol (e.g., *STA studies, condition charge of cell)*.

4. Set the temperature chamber to a constant temperature of 25 °C.

5. Remove the electrochemical cell from the glovebox and place it inside the temperature chamber. Plug in the appropriate cables to connect the cell to the cycler.

6. Run the procedure by selecting the file name of the protocol, entering the corresponding current for a C/20 C-rate and select the chamber number. Afterwards, click on the **Start** button.

7. Regularly check the charge/discharge versus time profile to identify any issues during cycling. To do this, select the channel and click on the graphic logo to display the graph. If the measured capacity differs more than 10% from the calculated capacity, do not use the cell because there were possibly unwanted reactions (that may subsequently modify the thermal data) or the cell assembly was unsuccessful.

8. Calculate the degree of graphite lithiation, using the following formula:

Degree of Gr lithiation (%) = (Experimental discharge capacity / calculated areal capacity) * 100

NOTE: The experimental discharge capacity is obtained from the second discharge step in paragraph 3.2. Indeed, the software indicates an experimental charge and discharge capacity for every cycle. The calculated areal capacity (mAh/cm^2) is obtained according to step 2.4.

4. Cell disassembly and preparation for STA/GC-MS/FTIR analysis

1. After the cycling step, bring the electrochemical cell inside the glovebox for disassembly. Open the cell, remove the plunger, take out one electrode (cathode or anode), and reassemble the cell to protect the remaining electrode from drying out.
2. Weigh the electrode using the precision balance from step 1.2.2 and place it on a fresh aluminum foil. Fold the foil and place it for 2 h in the transfer glove box antechamber under vacuum, to dry the electrode.

   NOTE: It was found *via* preliminary tests that a 2 h drying time was optimum to reach a stable weight. The stabilization criterion was the absence of significant weight fluctuation between two measurements of the electrode for a minimum time of 5 min. A fluctuation was considered significant when the weight varies more than the interval specified below:

   X mg ± 0.01 mg
3. When the weight has stabilized at X mg ± 0.01 mg, note the weight of the dried electrode. Proceed to the scratching of the disc electrode, using tweezers and a spatula, to harvest the coated material for further characterization.

5. Thermal characterization and gas analysis

NOTE: Thermal characterization and gas analysis are carried out in the set up as described in **Figure 1**.

1. **STA preparation**
   1. Create a new method by opening the STA software and clicking on **File**, and then on **New**. Under the **Setup** tab of the **Measurement Definition** window, select the parameters according to **Table 4**.
   2. Go to the **Header** tab and select **Correction** to execute a correction run with an empty crucible for baseline correction. Write the name of the sample (e.g., *correction run NMC-Gr-16_Gr*) and select the file for the temperature and sensitivity calibration to be used for the run. Go to **MFC gases** and select **Helium** as purge gas and protective gas.

      NOTE: The **Correction Run** is a run to establish an accurate baseline.
   3. Create the temperature program under the **Temperature Program** tab, as described in **Table 5,** to define the heating and cooling process.
   4. Set the flow rate of helium to 100 mL/min and 20 mL/min for purge and protective gas, respectively. Click on **GN2** (gas nitrogen) as cooling medium and **STC** for sample temperature control for all the segments of the temperature program, starting from the isothermal step at 5 °C to the end of the heating segment.
   5. Go to the **Last Items** tab and give a file name to this run (which could be the same as the sample name).
   6. Use the precision balance (the same balance as used in step 1.2.2) and measure the weight of the

empty crucible. Enter the crucible mass next to the name of the sample.

7. Open the silver furnace and place the crucible, together with the reference crucible, on the DSC/TG sample holder of the STA.
   NOTE: The crucibles are of aluminum with a laser-pierced lid with a hole of 5 µm diameter.

8. Make sure the sample holder is well-centered to avoid collision while closing down the furnace. To this end, lower down the silver furnace with caution and when the furnace is close to the sample holder, check the position of the sample carrier with respect to the internal walls of the silver furnace.

9. Evacuate the furnace (to remove argon) slowly and refill it with helium at maximum flow rate (350 mL/min purge gas and 350 mL/min protective gas). Repeat the evacuation/refill at least two times to get rid of the argon coming from the glove box atmosphere (when opening the furnace to place the crucibles).
   NOTE: The evacuation and backfilling step (the step of helium refilling) is important since the thermal conductivity from the STA furnace to the sample is influenced by the type of gas environment inside the furnace.

10. After the evacuation and refilling step, wait for 15 min to stabilize the weight. Execute the correction run, using the temperature program, by pressing **Measure** to start the run.

11. When the run is finished, take out the empty crucible. Put a sample mass, typically 6-8 mg, of the scratched material (anode or cathode) in the crucible. After weighing the sample in the crucible and recording the mass, seal the pan and lid using a sealing press.

12. Repeat steps 5.1.7 to 5.1.9 with the filled crucible.
    NOTE: The same crucible and lid must be used as in the correction run.

13. Open the correction run file by going to **File** and **Open**. Select **Correction > Sample** as measurement type under the **Fast Definition** tab. Write the name and the weight of the sample (e.g., *NMC-Gr-16_Gr*) and choose a file name.

14. Go to the **Temperature Program** tab and activate the **FT** (FTIR) option for the isothermal step of 5 °C and the heating segment to 590 °C in order to launch FTIR gas monitoring for these two segments. Tick the **GC** box for the heating segment (5 °C to 590 °C) to trigger GC-MS analysis.
    NOTE: Before launching the test, the coupled gas equipment needs to be prepared as explained in the corresponding section (i.e., sections 5.2 and 5.3) below.

2. **FTIR preparation**

   1. Take a funnel, insert it into the Dewar of the mercury cadmium telluride (MCT) detector port and carefully fill it with liquid N_2.

   2. Open the FTIR software. On the **Basic Parameter** tab, load the TG-FTIR method called *TGA.XPM*. The input measurement parameters used for this method are referred to in **Table 6** (see also **Supplementary File 2** for the parameter-screenshots of TGA.XPM program).
      NOTE: Ensure a constant argon gas flow rate with a mass flow meter placed at the inlet of the IR gas cell. When not in operation, a flow of 10 L/h is needed to

remove the presence of moisture and CO_2. During operation, a flow of 20 L/h is used. The 10 cm path IR gas cell is an external gas cell (heated here at 200 °C) coupled to the STA to identify evolved gases during thermal analysis.

3. Check the interferogram by clicking on the **Check Signal** tab. Wait until interferogram has stabilized before starting the thermal analysis.

3. **GC-MS set up**

1. Put the following parameters in the GC-MS method for the online gas monitoring, as shown in **Table 7**.
2. Turn on the vacuum pump line to draw evolved gaseous species from STA to FTIR and GC-MS. Adjust the pumping rate to a stable flow, which is approximately 60 mL/min.
3. After loading the method with the above mentioned parameters (see **Table 7**), click on **Start Run** and fill in the sample name and data file name; then, click on **OK**, and then on **Run Method**.

4. **Launch of STA/GC-MS/FTIR run**

1. In the STA software, verify the temperature program, the gas flow, and make sure the GC-MS and FTIR options are enabled.
2. Press **Measure** and click on **Start FTIR Connection** to establish the connection between STA software and FTIR software.
3. Once the connection is established, click on **Tare** to put the balance at zero and check the gas flow by selecting **Set Initial Gases**. The flow of the purge gas in the sample compartment should be at 100 mL/min and the flow of the protective gas should be at 20 mL/min.
4. Press the **Start** button to launch the run.

NOTE: Repeat the thermal characterization and evolved gas analysis with anode and cathode materials at 5, 10, and 15 °C/min.

5. **DSC and TGA data evaluation**

1. After the experiment is completed, open the Netzsch Proteus data treatment program by double-clicking on the icon.
2. On the above ribbon bar, select **T/t** with an arrow beneath to put the temperature scale (T) on the x-axis instead of time (t). For clarity, remove the cooling curves by clicking on the **Segment** button on the ribbon bar and by deselecting them. Also, remove the sample compartment gas flow, the TGA, and the Gram-Schmidt curves by pressing on the **Axes/Curves** icon, and then untick them.
3. Measure the total heat release and the areas of each major DSC peak by right clicking on the graph, and then select **Evaluate**. Afterwards, click on **Partial Area** and select the temperature range where the total heat release will be measured, using **Linear** as baseline type. Regarding the partial area preferences, select **Left Started**.
    1. Then, move the cursor and click at the end of each major DSC peak to measure the heat release related to them and press apply.

    NOTE: A peak ends when the signal returns to the baseline.
4. Measure the peak temperature of each major peak (3 in the graphite anode and 3 in the NMC (111) cathode) by right clicking on the DSC graph and go to **Evaluate > Peak**.

1. Then, move the cursor at each end of the major DSC exothermic peak and click to determine the peak temperature.

5. Collect the values of peak temperature, heating rate, and heat flow for each peak and the total heat flow. Plot the peak temperature vs heating rate in a graph.
NOTE: From the DSC experimental data, Kissinger analysis is used to calculate the activation energy for the peaks that are following an Arrhenius-type kinetic.

6. Put the TGA curve back into the graph by selecting the **axes/curves** icon and ticking the **TG** box.

7. Assess the mass loss versus temperature, in parallel with the DSC curve, for a first evaluation of the phase transition/enthalpy changes correlated with the TGA curve. To this purpose, right click on the TGA curve, and then select **Evaluate > Mass Change**. Move the cursors before and after the weight loss, press **Apply**, and then **OK**.

8. Switch the X-axis from temperature to time scale.

9. Check the evolved gases by clicking on the **GC-MSD Netzsch data analysis icon** in the GC-MS station. Load the data file of the corresponding thermal analysis and check the GC peaks.

10. Enlarge the peak to be analyzed and, subsequently, right-double click on the baseline and the peak. Afterwards, go to the icon bar and select **Spectrum > Subtract**. This will subtract the baseline from the spectrum.

11. Double-click on the MS graph to check the potential candidates/matches corresponding to the peak in the NIST database.

NOTE: There is a difference in the time scale between the GC-MS analysis and the STA analysis. Indeed, the GC-MS is always launched 20 min after the initial start of the thermal program. The GC-MS monitoring starts at the beginning of the STA heating phase from 5 °C to 590 °C. The initial temperature of the GC-MS is 100 °C and the initial temperature of the STA heating segment is 5 °C.

12. Regarding the FTIR data evaluation, open the **Opus** software. Load the spectra recorded during the experiment by going to **File** on the ribbon tools, and then selecting **Load File** and retrieve the data file from the folder. Now, **TRS (time-resolved spectra) Postrun Display** is open.
NOTE: The 3D data visualization allows displaying the IR spectra collected at different wavelength number (cm^{-1}) as a function of time (seconds), showing the gaseous products detected by the FTIR spectrometer coming from the thermal decomposition of electrode material in the STA. The Y-axis shows the amplitude of the absorbance signal; Z-axis, the time and X-axis the wavenumber.

13. On the 2D (2 dimension) DSC curve located on the right side of the 3D graph, change the X-axis from time to temperature by pressing the right button of the mouse and go to **Select Time Axis** and select **Temperature**.

14. Afterwards, on the same 2D DSC graph, move the blue arrow cursor along the X-axis (temperature) of the DSC curve to monitor the variation of IR absorption over a wide wavenumber range, displayed on the right bottom window (IR absorbance intensity versus wavenumber cm^{-1}).

After this assessment, identify a group of absorption bands that shows similar trend (same number of maxima at the same temperature), then position the blue arrow cursor in a location that reflects maximum absorption of these bands.

NOTE: This step allows the determination of IR absorption bands corresponding to evolved gas compounds, associated to a given temperature range."

15. On the IR absorbance spectrum window, the blue (unknown) and the red (baseline) absorbance curves from the selection in the 2D DSC curve are displayed. Identify the various absorption peak positions of the blue IR spectrum (unknown spectral data) by moving the green and fuchsia arrow cursors along the X-axis (wavelength number cm^{-1}).

16. On the scan list located in the middle window, the temperature, date/time and index info are displayed for each spectrum. Scroll down the list to find the red and blue scans that are highlighted with the same color code.

17. Extract the red spectrum (baseline) by first right clicking on the list and select **Extract Selected Spectra**. Repeat the same operation with the blue spectrum scan. On the **Display** tab, the extracted spectra are shown with their index number and temperature info.

18. On the OPUS browser located at the left side of the window, click on the file name of the spectrum scan (the unknown spectrum) and press the subtraction icon to open the **Spectrum Subtraction** window. In the OPUS browser, click on the AB icon from the baseline file and drag it inside the **File(s) to Subtract** box. In the **Frequency Range** tab for subtraction, tick the **Use File Limits** box.

19. Click on **Start Interactive Mode**. Now, the window is showing two graphs. The upper one displays the unknown spectrum (in red now instead of blue) and the baseline to be subtracted (in blue now). The graph located at the lower part of the window is the resulting curve from the subtraction operation. Click on **Auto Subtract**, and then on **Store** when finished. After this operation, the following icon SUBTR is then added to the unknown absorbance spectrum file in the OPUS browser, showing that spectrum has been processed.

    NOTE: The **Changing Digit** option allows to customize and optimize the subtraction constant that is set to one by default. In case of doubt, select **Auto Subtract** and the software will do it automatically.

20. Close the baseline file from the OPUS browser to remove it from the graph.

21. Select the unknown absorbance spectrum file from the OPUS browser and click on the **Spectrum Search** icon from the ribbon tool bar. In the **Search Parameters** tab, put the value of 30 as the **Maximum Number of Hits** and the value of **100** for the **Minimum Hit Quality**. Tick the box of **Several Components** to be searched in the spectrum. In the **Select Libraries** tab, make sure the relevant library called **EPA-NIST Gas Phase Infrared Database** is present. If not, add it to the library. After making all the settings, click on **Search Library**. A list of potential matches is listed after this action.

22. Check the list of potential gaseous compounds present in the unknown IR absorbance spectrum

(which was selected by the blue cursor in step 5.14). By visual inspection, compare the frequency features from the different analyte reference spectrum (from the potential candidate compounds) with the unknown spectrum. Look for the best peak matches to identify the gas species released at a given temperature.

23. Select the most representative wavenumbers of each identified gas compound. The time-intensity diagram in the top right corner can be used to measure the concentration variation of the generated gases.

24. Export the gas evolution data for the different identified gases (in this case, CO_2 and EC) as ASCII format for further processing in Excel, Origin, or other data processing software. For this purpose, go to the **TRS Postrun-Display** window.
NOTE: In the upper right window, two wavelengths are present on the list. One corresponds to the green cursor arrow and the other one to the pink cursor arrow, both from the absorbance graph (of a given temperature) in the bottom right section. In this case, the wavelengths of the absorbing peaks shown by the green and pink arrows correspond to EC with 1,863 cm^{-1} and the CO_2 with 2,346 cm^{-1}.

25. Select one wavelength, right-click, and go to **Export Trace > Plain ASCII (z, y)**. Repeat the same process with the other wavelength.

Representative Results

Figures shown in this section have been taken from reference[48].

Electrochemical characterization of electrochemical cells

A total of twelve cells were electrochemically characterized before the thermal experiments and the results are shown in **Table 8**. The capacity for each cell was calculated (see **section 2** of the Protocol) taking into consideration the active material mass and assuming a theoretical capacity of 145 mAh/g for NMC (111) and 350 mAh/g for graphite. The experimental discharge capacity was obtained from the second discharge step. **Table 8** also shows the degree of lithiation, calculated following section 3.8.

The loading of the graphite anode was designed by the manufacturer to have a 10% excess active material compared to that of the cathode to avoid lithium plating in the two electrode NMC (111)/Gr cell configuration. Our measurements showed an excess of 11% in average.

The charge and discharge potential profiles for the second cycle of NMC (111)/Gr electrochemical cell, sample number 5 from **Table 8**, are presented in **Figure 3**. This graph shows that the discharge curve stops at an anode potential of circa 50 mV vs Li, which therefore confirms the absence of lithium plating. Indeed, the anode potential does not reach 0 V vs Li.

Thermal decomposition of lithiated graphite

Based on our experimental measurements and observations, possible thermal decomposition mechanisms for the graphite anode are identified from the summary of the literature survey listed in **Table 1**, **Table 2**, and **Table 3** and discussed later in the discussion section.

A typical thermal decomposition profile of the powder scratched from the anode (sample number 5 from **Table 8**) is shown in **Figure 4a**. The heat flow (mW/mg), mass loss (wt%), and the relative FTIR intensity of CO_2 (2,346 cm^{-1})

and EC (1,863 cm^{-1}) are displayed as a function of the temperature (from 5 °C to 590 °C obtained at 10 °C/min heating rate). The decomposition profile can be split into four distinct thermal regions (shown by Arabic numerals). The most prominent peaks in the DSC curve are indicated with roman numerals. The FTIR spectra of the evolved gas at 110 °C and 250 °C are shown in **Figure 4b** and **Figure 4c**, respectively. For comparison purposes, the NIST reference spectra of CO_2, ethylene, and EC are added in the figures.

A sharp endothermic peak is visible in region 1. In this temperature range below 100 °C, no mass loss was detected nor gas generated. Interestingly, this peak is also found with pristine graphite electrode in contact with electrolyte (not shown) without prior electrochemical cycling. This observation suggests that this peak does not belong to the thermal characteristics of lithiated graphite. For this reason, it has not been taken into account for the calculation of thermal properties at a later stage.

Region 2 shows that with increasing temperature, a broad DSC heat decomposition, with a peak around 150 °C-170 °C (peak I.), is observed. The characteristic IR absorption of CO_2 (2,346 cm^{-1}) is seen around 100 °C and appears in parallel or after the onset temperature of the broad exothermic peak. **Figure 4b** shows the FTIR spectra at 110 °C where CO_2 is clearly visible. It was also detected by GC-MS in **Figure 5**. However, its peak intensity drops, as evidenced by absorption at 2,346 cm^{-1} in **Figure 4a**. Furthermore, EC starts to evaporate near 150 °C, as highlighted by the FTIR 1,863 cm^{-1} curve in **Figure 4a**. Gas evolution and mass loss in the temperature range 100 °C-220 °C is minimal. At the end of region 2, it is worth noting a small endothermic peak around 200 °C after the mild heat release. The possible origin of this phase transition is provided later in the discussion section.

As can be seen in region 3, as the temperature rises beyond 220 °C, the heat generation increases, as highlighted by a sharp exothermic peak (peak II), associated with significant mass loss and simultaneous gas evolution. Gas analysis shows clearly CO_2 (*via* FTIR in **Figure 4a** and GC-MS in **Figure 5**), EC (*via* FTIR **Figure 4a** and **Figure 4c**), PF_3 (*via* GC-MS in **Figure 6**) and ethylene (*via* GC-MS in **Figure 7**) as major gaseous products of thermal reactions. It should be mentioned that in the profile of the infrared spectra at 250 °C (**Figure 4c**), it is difficult to assign all the absorption bands due to the complexity of the IR pattern compared to the one obtained at 110 °C (**Figure 4b**). The features observed in this region, notably the change in gas evolution compared to region 2, suggest consecutive and parallel decomposition mechanisms.

As the temperature exceeds 280 °C, the amount of heat release decreases with small, partly overlapping peaks visible in region 4. TGA data reveals small changes in mass loss with gas products generated and identified only at 15 °C / min. With GC-MS, traces of ethylene in **Figure 7**, C_2H_6 in **Figure 8**, CH_4 (measured but not shown), C_3H_6 (measured but not shown) were observed. The gaseous decomposition species and the smaller amount of heat released (from these overlapping exothermic peaks), compared to region 3, indicates that the thermal processes occurring in this region are different from the previous ones. Furthermore, it should be noted that the more stable decomposition products formed at previous thermal stages might also start to decompose in this temperature range. Between 400 °C-590 °C, decomposition reactions leading to enthalpy changes are not observed.

Figure 9 shows the thermal decomposition profile of lithiated graphite at three different heating rates (5, 10, and 15 °C/ min). The kinetic analysis applied here, namely Kissinger

method based on Arrhenius equations, derives activation energy and frequency factor based on the peak maximum temperature for each heating rate. The DSC curves reveal that higher heating rates result in higher peak temperature except for peak I. The maximum peak temperature for the latter shifts to lower temperature with the increase of heating rate. This observation suggests that Peak I does not follow an Arrhenius-type kinetic and consequently, the Kissinger method is not applicable. The small, partly overlapping exothermic peaks visible in Peak III show a moderate change in shape with a sub-peak becoming more pronounced and sharp at higher heating rate. This probably implies an influence of the reaction products of region 2 and 3 on Peak III (located in region 4). However, it is notable that the Kissinger analysis can be applied in this case.

The Kissinger plots acquired from DSC analysis of Peak II and Peak III are shown in **Figure 9**. All DSC experiments were repeated at least three times per heating rate (see **Table 8**). Regarding Peak II, NMC-Gr-23 has been identified as an outlier because it is outside the confidence of prediction of other data, assuming normal distribution. Therefore, this data has been discarded from further calculation to determine the kinetic parameters (activation energy, frequency factor, heat release) of Peak II, but not of Peak III. Indeed, in Peak III, NMC-Gr-23 is within the confidence of prediction, as illustrated in **Figure 9**. Despite the partly overlapping multistep thermal decomposition of Peak III, the linear Kissinger relationship is still applicable in these exothermic reaction processes happening in region 4.

The identified kinetic parameters for the lithiated graphite are listed in **Table 9**. Values of heat release, activation energy and frequency factor for Peak I have been extracted from literature[34]. From these data, the simulation of the DSC profile was conducted for the anode by building an approximate kinetic model to describe the decomposition reactions occurring in this electrode chemistry. The description of the identified decomposition paths that were taken into account for the modeling are specified in the discussion section.

Thermal decomposition of NMC(111) cathode

The thermal behavior and stability of the cathode material was investigated following the same approach as for the anode. The main reaction mechanisms were identified from **Table 1**, **Table 2**, and **Table 3** and are discussed at a later stage.

A representative thermal decomposition profile of the powder scraped from the cathode (sample number 5 from **Table 8**) is depicted in **Figure 10**. The heat flow (mW/mg), mass loss (wt.%), and the relative FTIR intensity of CO_2 (2,346 cm^{-1}) and EC (1,863 cm^{-1}) as a function of the temperature (from 5 °C to 590 °C at 10 °C/min heating rate) are displayed in the graph. When comparing anode and cathode DSC profiles, there is a difference between the amount of heat generated, with a heat release that is larger for the anode. This suggests that the negative electrode is more thermally reactive. It also indicates that the anode thermal events contribute in a more significant way to the heat release than the cathode. Four thermal regions were identified in the thermal decomposition graph of delithiated NMC (111) cathode material (shown with Arabic numerals).

In region 1, below 150 °C, a small endothermic peak is visible around 70 °C, as observed in the anode, though less intense. In addition, minor CO_2 evolution above 100 °C, without significant change in the heat flow behavior is observed and almost identical to the one displayed in **Figure 4a**. The occurrence of this endothermic phenomenon and

CO_2 evolution in both positive and negative electrodes may stem from similar decomposition reactions. Therefore, this peak can be neglected from further considerations in the subsequent analysis and calculations.

As the temperature enters the 155 °C-230 °C range in region 2, there is an increase in the EC FTIR absorption curve in **Figure 10**. The DSC plot reveals a small endothermic peak around 200 °C that is more obvious at 15 °C/min in **Figure 11**. This overlaps with exothermic decomposition reactions, which makes separate evaluation difficult. For practical reason, this peak cannot be included in the calculation of thermal triplets. It should be noted that the TGA profile in this temperature zone displays a rapid mass loss that could be correlated with the evaporation of EC.

Region 3 is characterized by a sharp exothermic peak with a sudden increase of CO_2 and a continuous drop of EC, as shown by FTIR signal intensity between 240 °C and 290 °C. TGA results suggest a minor mass loss related to this region.

Between 290 °C and 590 °C, three consecutive exothermic decomposition processes take place that involve coinciding evolution of CO_2 for each exothermic peak. These thermal processes in region 4 cause continuous mass loss that does not seem to stop beyond 590 °C, as shown by the TGA weight loss profile.

To investigate kinetic parameters of cathode thermal decomposition, DSC measurements were performed at 5, 10, and 15 °C/min. As can be noted in **Figure 11**, the increase of heating rate leads to a shift of the peaks to higher temperatures. This demonstrates the suitability of Arrhenius-type kinetic and Kissinger analysis to describe these thermal reactions. The thermal triplets of NMC Peaks I-III are calculated and the Kissinger plots are shown in **Figure 11**.

Results from Peak I in **Figure 11** show clearly that NMC-Gr-30 happens to be an outlier since this data falls out of the confidence of prediction band of the other data. For this reason, it has been discarded for the subsequent analysis. Good linear fits with all data were obtained for Peak II and Peak III in **Figure 11**. NMC-Gr-30 was not considered as an outlier in Peak II and Peak III because NMC-Gr-30 falls within the confidence of prediction in both cases, as shown in **Figure 11**. From the slope of the Kissinger plots, the activation energy can easily be calculated.

Table 10 shows the kinetic parameters and their relative errors of Peak I, Peak II, and Peak III, assuming normal distribution. Regarding the electrolyte, especially EC since DMC is expected to evaporate fully (due to its low boiling point of 90 °C at 760 mm Hg), the kinetic parameters of simultaneous processes of EC evaporation, EC combustion and EC decomposition happening in regions 2 and 3 are listed in **Table 11**. With respect to EC evaporation,the activation energy and frequency factor were determined from the derivative thermogravimetry (DTG) plots at different heating rate. DTG graph depicts the mass loss upon heating versus temperature and DTG peak shifts to higher temperature as the heating rate increases (measured but not shown). Furthermore, this observation shows that EC evaporation happens faster than EC reaction with NMC. Therefore, the Kissinger method was used to calculate the kinetic parameters of EC evaporation, taking the heat of evaporation of EC from the NIST database. As for EC combustion, the data were approximated from Reference[69,70]. Regarding EC decomposition, the thermal parameters were taken from Reference[71].

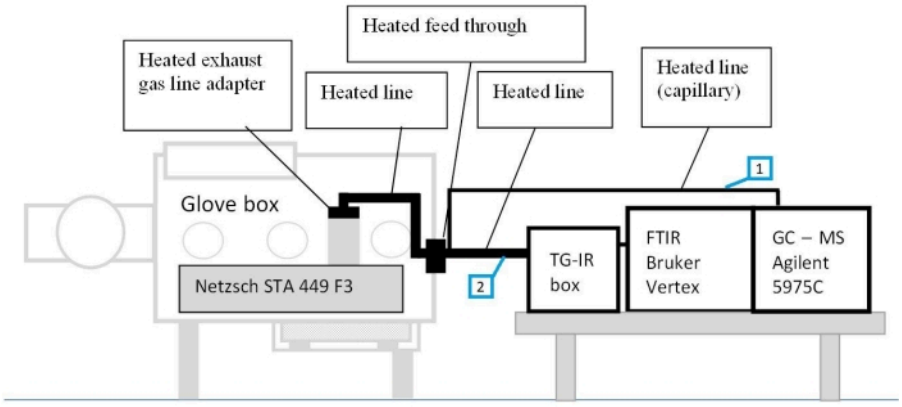

Figure 1: The set-up of the coupled measurement system. 1-coupling line between STA and GC-MS; 2-coupling line between STA and FTIR system with TG-IR box. The figure is reproduced with permission from Reference[48]. Please click here to view a larger version of this figure.

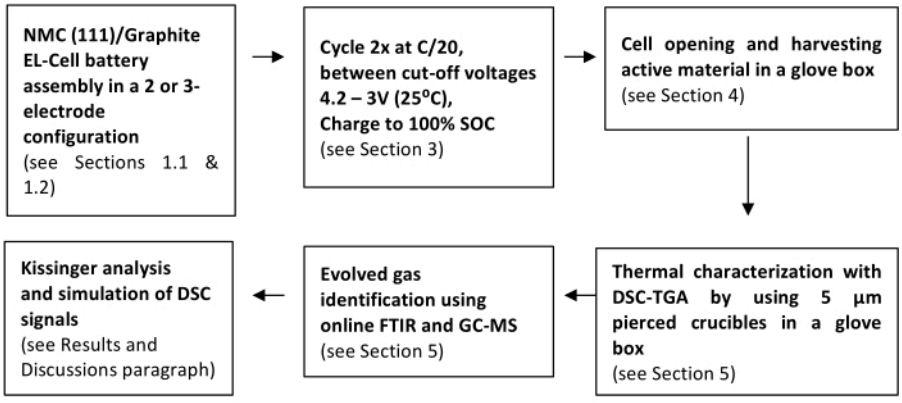

Figure 2: Schematic representation of the steps described in the protocol. Please click here to view a larger version of this figure.

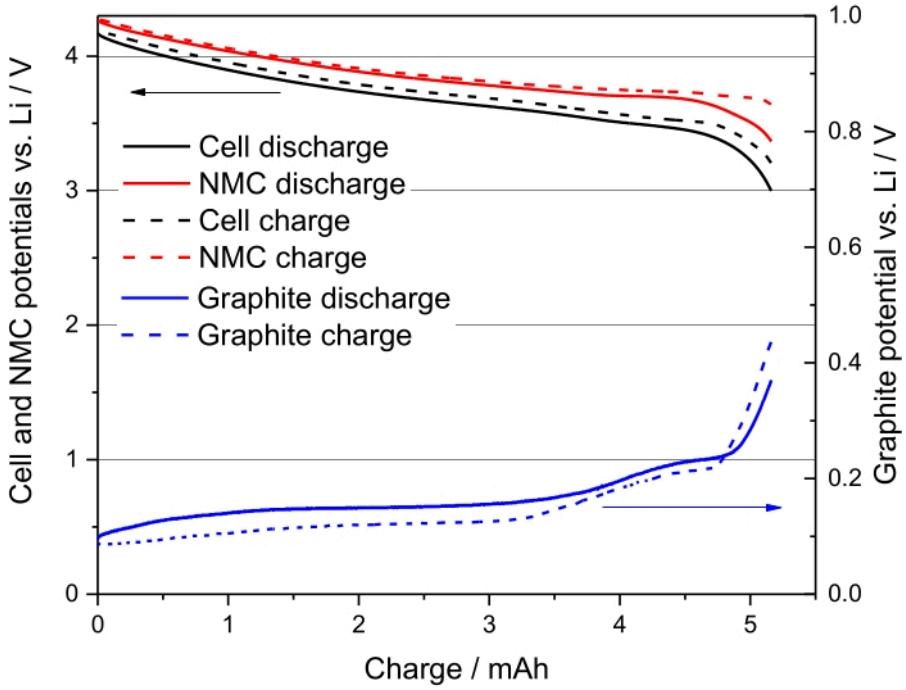

Figure 3. The second cycle of sample number 5, in Table 8, namely NMC-Gr-30 at C/20. Reproduced with permission from Reference[48]. Please click here to view a larger version of this figure.

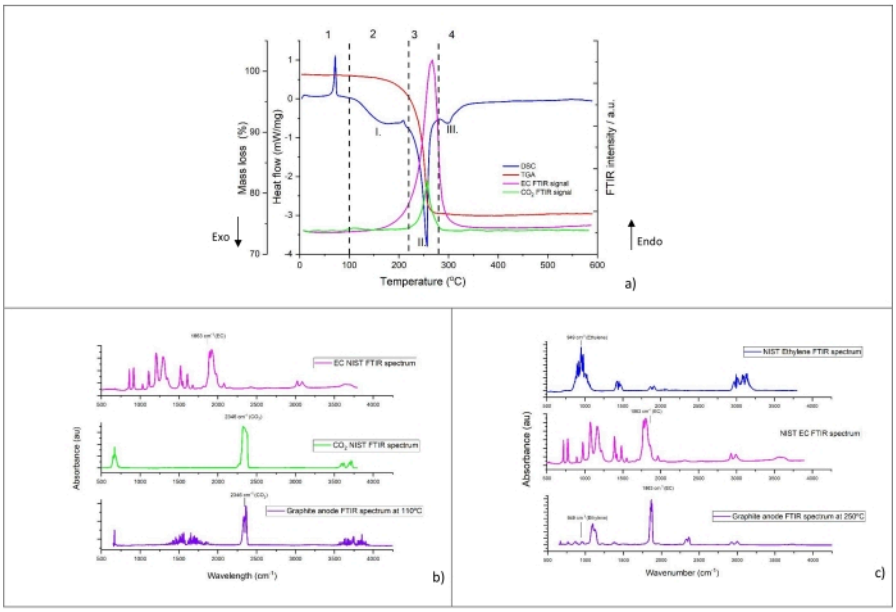

Figure 4: TGA, DSC, and FTIR signals for lithiated graphite number 5 in Table 8, namely NMC-Gr-30. (**a**) Simultaneous thermal and FTIR analysis signals of lithiated graphite with FTIR absorbance peaks recorded at 1,863 cm^{-1} for EC and 2,346 cm^{-1} for CO_2, (**b**) FTIR spectra of the gases evolved from lithiated graphite recorded at 110 °C, (**c**) FTIR spectra of the gases evolved from lithiated graphite recorded at 250 °C. Heating rate for this experiment was 10 °C/min. The reference spectra are plotted on the basis of the data from NIST Chemistry WebBook[68]. Arabic numerals represent the different thermal regions, which may consist of several peaks. Roman numerals show the most prominent and modeled peaks. This figure is reproduced with permission from Reference[48]. Please click here to view a larger version of this figure.

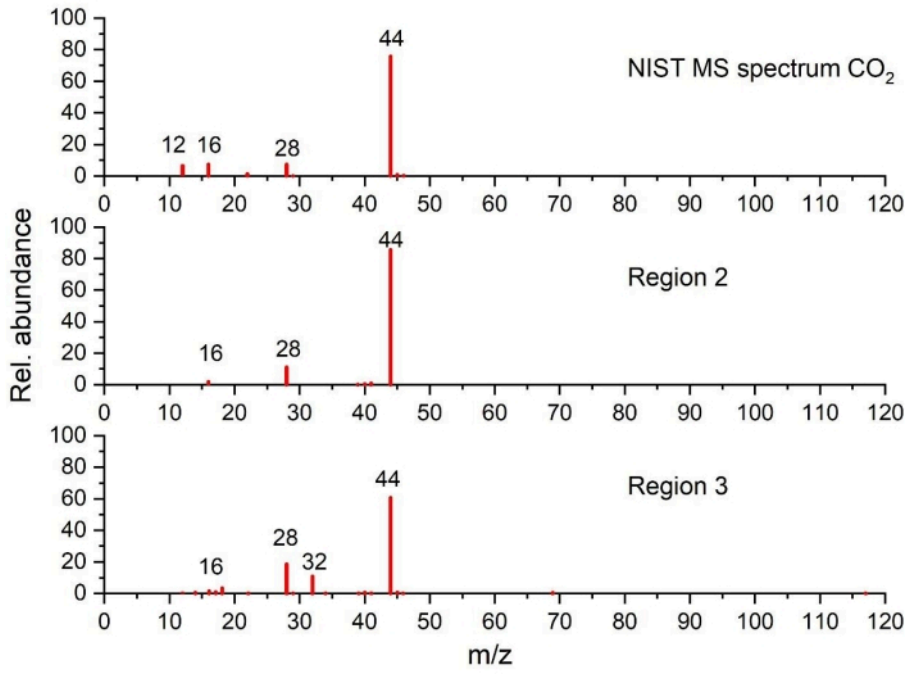

Figure 5: Mass spectra of CO_2 detected in regions 2 and 3 as compared to NIST spectrum (plotted on the basis of the data from NIST Chemistry WebBook[68]). Please click here to view a larger version of this figure.

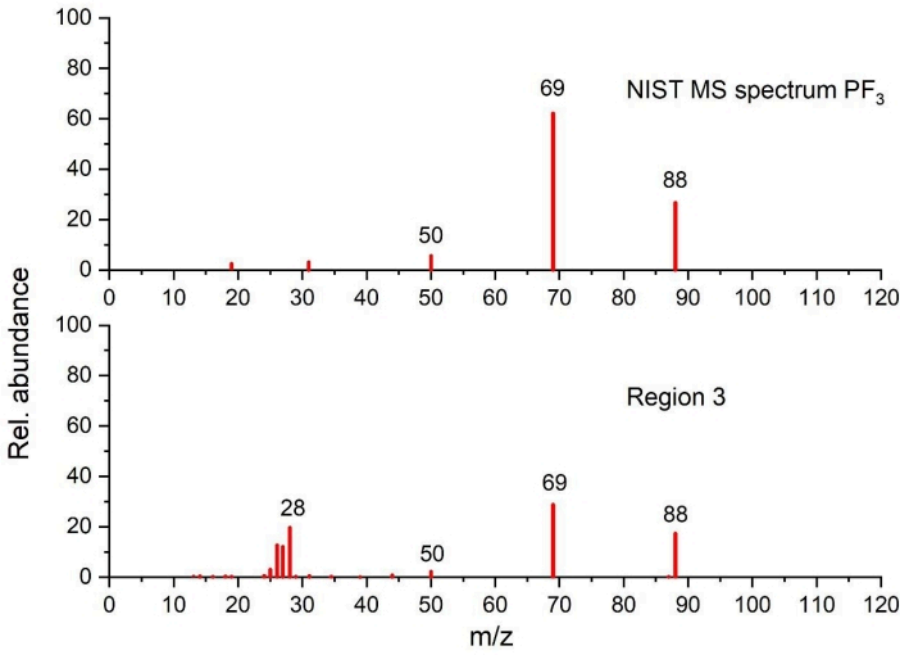

Figure 6: Mass spectrum of PF_3 detected in the temperature region 3 as compared to NIST spectrum (plotted on the basis of the data from NIST Chemistry WebBook[68]). Please click here to view a larger version of this figure.

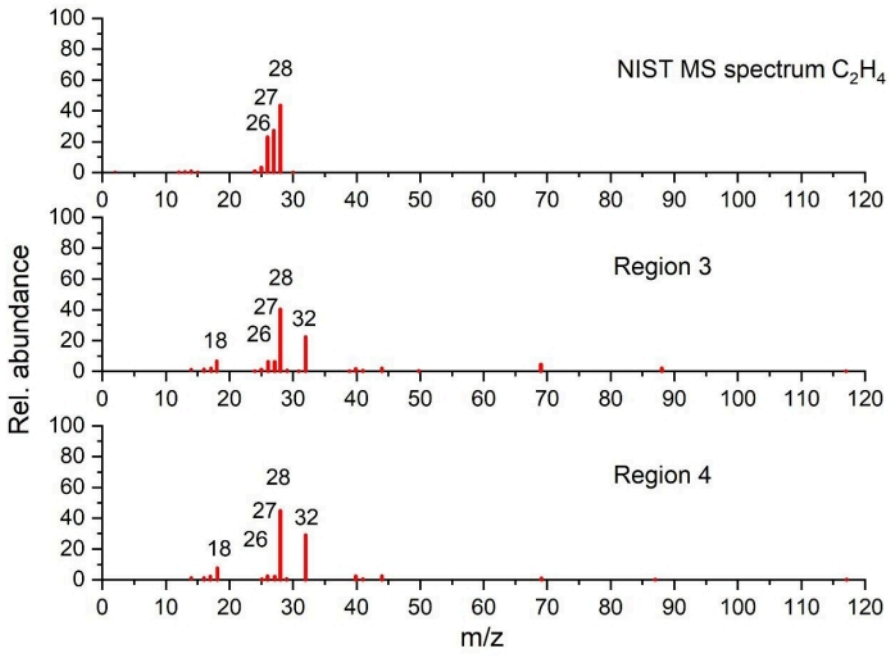

Figure 7: Mass spectra of ethylene detected in the temperature regions 3 and 4 as compared to NIST spectrum (plotted on the basis of the data from NIST Chemistry WebBook[68]). Please click here to view a larger version of this figure.

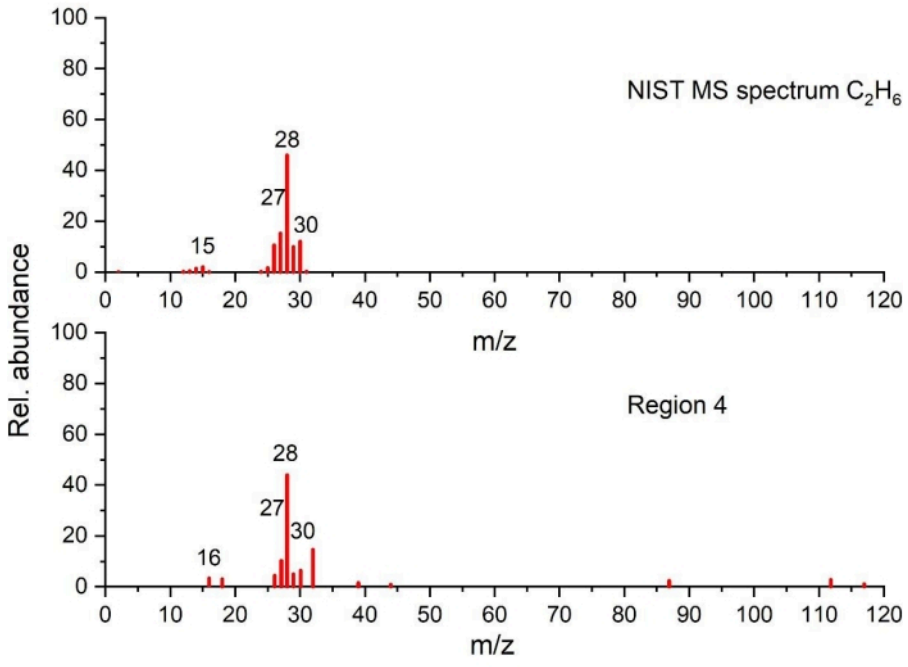

Figure 8: Mass spectrum of C_2H_6 detected in the temperature region 4 as compared to NIST spectrum (plotted on the basis of the data from NIST Chemistry WebBook[68]). Please click here to view a larger version of this figure.

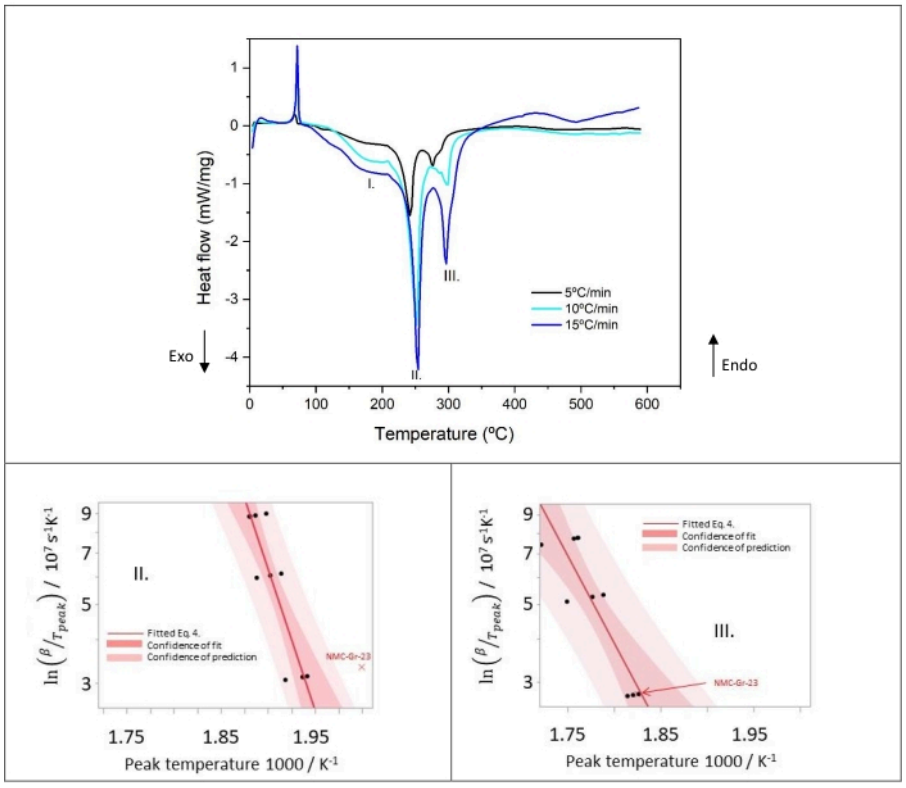

Figure 9: Heat flow of lithiated graphite at heating rates of 5, 10, and 15 °C/min of samples number 2, 6, 9 in Table 8 and Kissinger plots of peaks II and III. This figure is reproduced with permission fromReference[48]. Please click here to view a larger version of this figure.

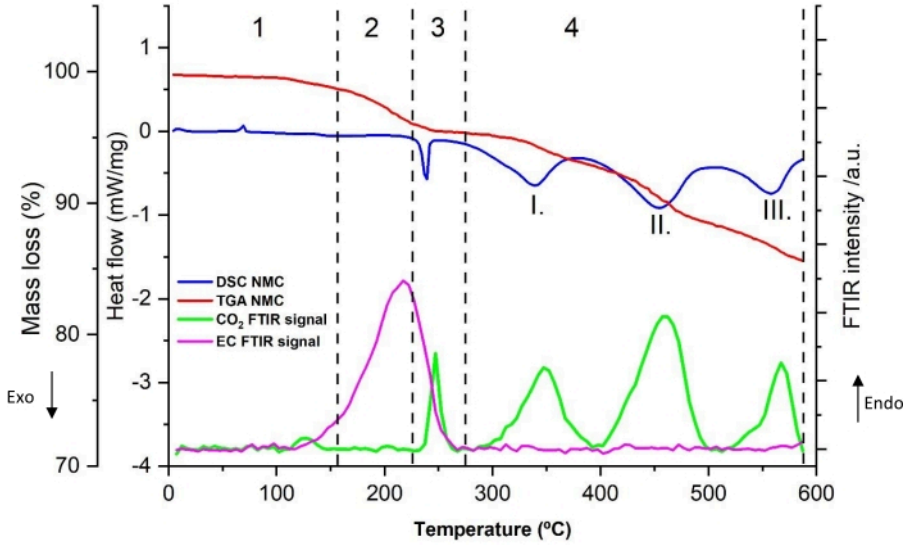

Figure 10: TGA, DSC, and FTIR signals for lithiated graphite number 5 in Table 8, namely NMC-Gr-30, with FTIR absorbance peaks recorded at 1,863 cm^{-1} for EC and 2,346 cm^{-1} for CO_2. This figure is reproduced with permission from Reference[48]. Please click here to view a larger version of this figure.

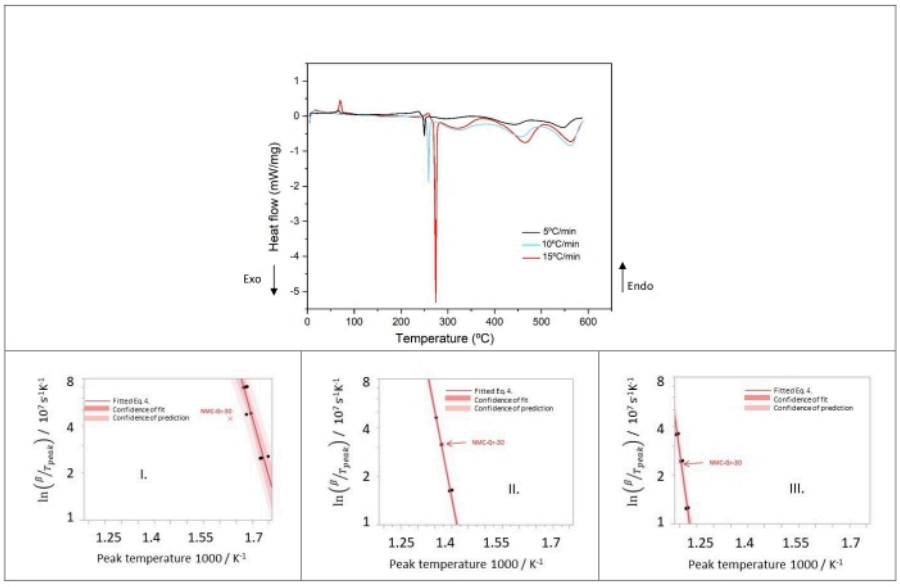

Figure 11: Heat flow of delithiated cathode at heating rates of 5, 10, and 15 °C/min of samples number 1, 5, 9 in Table 8 and Kissinger plots of peaks I, II, and III. This figure is reproduced with permission from Reference[48]. Please click here to view a larger version of this figure.

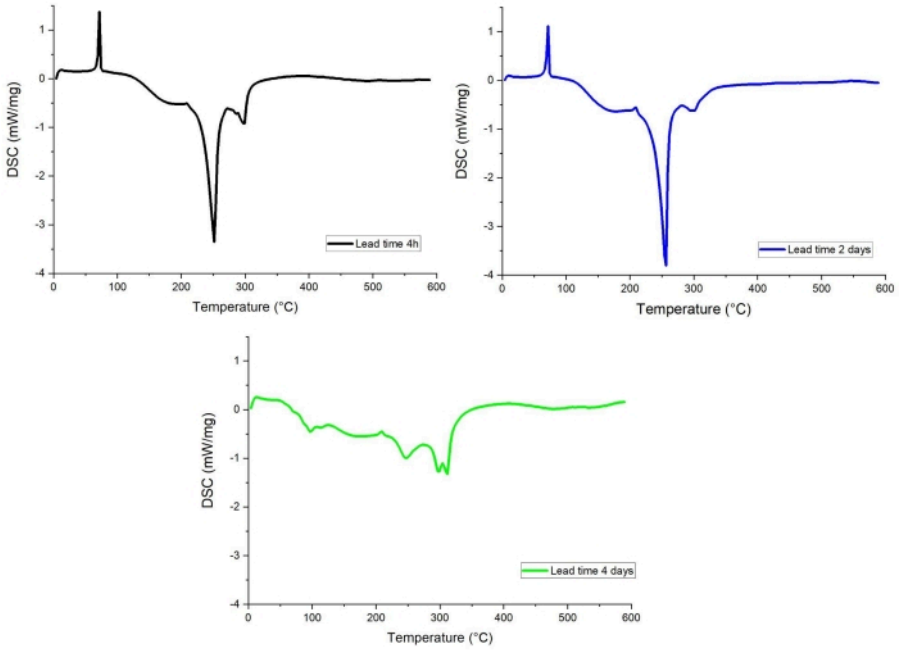

Figure 12: DSC profiles of graphite extracted from cells. (black) Lead time 4 h, (blue) Lead time 2 days, (green) Lead time 4 days. Please click here to view a larger version of this figure.

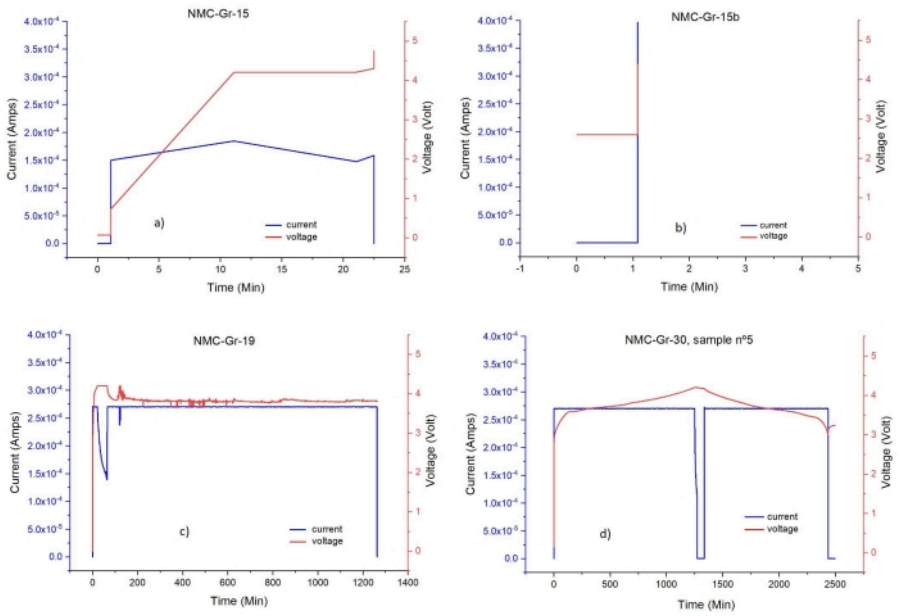

Figure 13: Voltage-time and current-time profiles of various EL cells. (**a**), (**b**), (**c**): cycling signature of not-properly assembled/closed/connected cells, (**d**) cycling signature of properly assembled/closed/connected cell. Please click here to view a larger version of this figure.

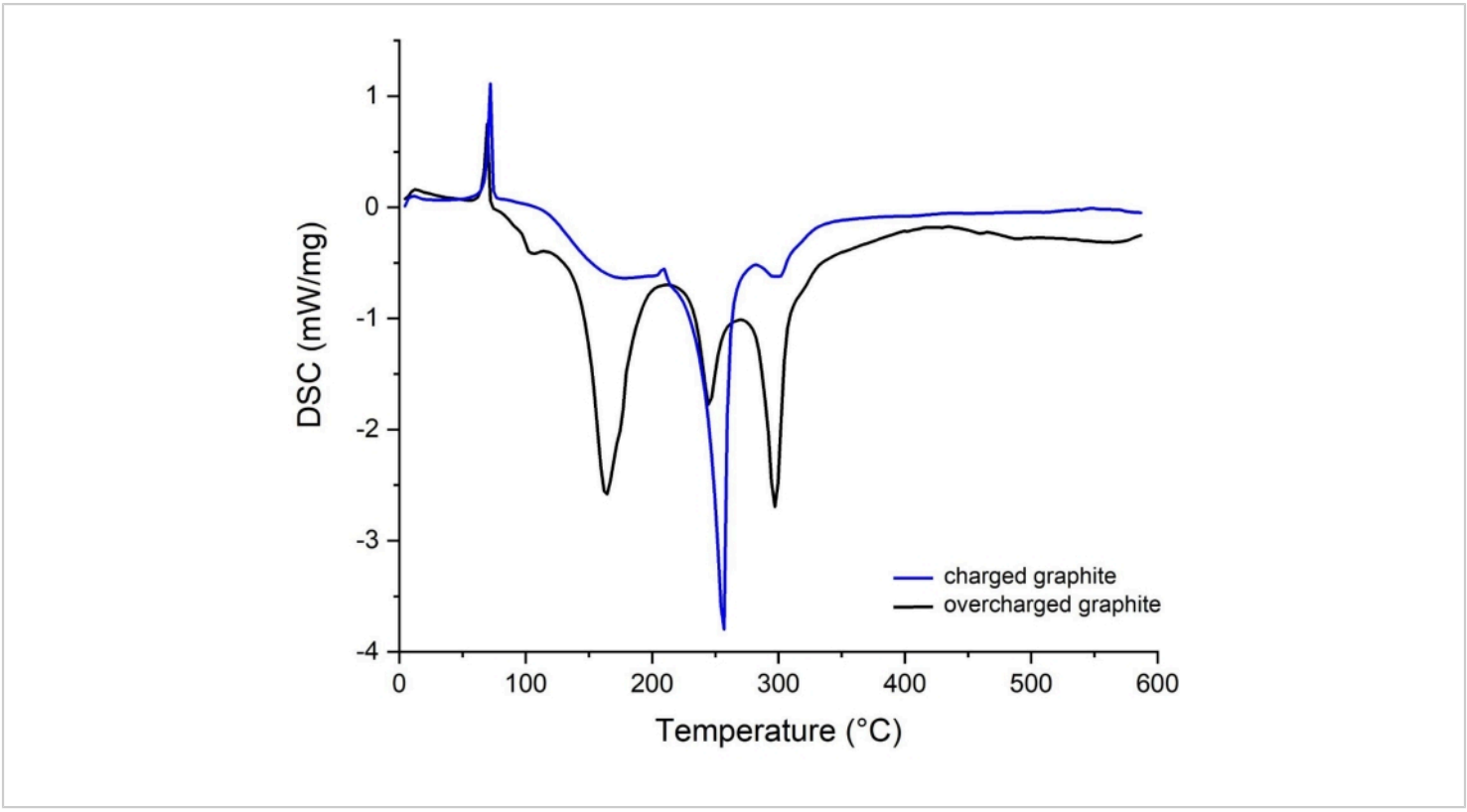

Figure 14: DSC spectra of graphite from capacity balanced and unbalanced cell. (blue) charged, (black) overcharged. Please click here to view a larger version of this figure.

Table 1: Anode decomposition reactions (at elevated temperature) identified in literature. EC: Ethylene carbonate, CMC: carboxymethylcellulose, R: low-molecular-weight alkyl group, SEI: solid electrolyte interface, p-SEI stands for the primary SEI developed during electrochemical cycling and s-SEI for secondary SEI, which may form at elevated temperature at the beginning of TR. Ethylene carbonate (EC) and dimethyl carbonate (DMC) are the solvents used in the electrode. Carboxymethyl cellulose (CMC) is the binder material. This table is reproduced with permission from Reference[48]. Please click here to download this Table.

Table 2: Identified decomposition reactions of NMC(111) de-lithiated cathode. NMC: Lithium Nickel Manganese Cobalt, HF: Hydrofluoric acid.This table is reproduced with permission from Reference[48]. Please click here to download this Table.

Table 3: Identified decomposition reactions of 1M $LiPF_6$ in EC/DMC = 50/50 (v/v) electrolyte. PEO: Fluoro-polyethylene oxide.This table is reproduced with permission from Reference[48]. Please click here to download this Table.

Table 4: Parameters used on the Setup tab of the Measurement Definition window of the STA. Please click here to download this Table.

Table 5: Temperature program for STA measurements with a heating rate of 10 °C/min. Please click here to download this Table.

Table 6: TG-FTIR spectroscopy measurement settings for the identification of evolved gases. Please click here to download this Table.

Table 7: GC-MS parameter settings for the qualitative measurement of emitted gases. Please click here to download this Table.

Table 8: Testing matrix for the STA experiments and the investigated cells' main electrochemical properties. The calculated capacity uses the measured mass loading of active material for each electrode and the rated capacity as provided by the manufacturer. The experimental discharge capacity is calculated from the second discharge cycle. n.a. = cycling file corrupted; therefore, the SOC calculation was not possible, but STA was performed. *scratched sample lost during preparation. The loading of the graphite anode was designed by the manufacturer to have a 10% excess active material compared to that of the cathode to avoid lithium plating in the two electrode Gr/NMC (111) cell configuration. Our measurements showed an excess of 11% in average.This table is reproduced with permission from Reference[48]. Please click here to download this Table.

Table 9: Determined thermal triplets and standard error (st.err.) of the lithiated graphite decomposition reactions. The Kissinger method was used to calculate the kinetic parameters (heat release, activation energy, and frequency factor) and their uncertainties. Since the Kissinger method is not applicable for Peak I, the data were extracted from literature.This table is reproduced with permission from Reference[48]. Please click here to download this Table.

Table 10: Determined thermal triplets and standard error of the delithihated NMC(111) decomposition reactions. Standard error appears in brackets. Kissinger method was used to calculate the kinetic parameters (heat release, activation energy, and frequency factor) and their uncertainties. This table is reproduced with permission from Reference[48]. Please click here to download this Table.

Table 11: Kinetic constants of EC evaporation, decomposition and combustion. The evaporation of EC is measured in this work and the calculated data and the standard error in bracket are given. The combustion is estimated from Reference[69,70] and the decomposition data is based on literature values[71].This table is reproduced with permission from Reference[48]. Please click here to download this Table.

Supplementary file 1: screenshot of electrochemical procedure in Maccor cycler. Please click here to download this File.

Supplementary file 2: screenshot of parameters from TGA.XPM program. Please click here to download this File.

Discussion

In the section below, the reaction mechanisms are identified and discussed for each electrode, based on the results collected from the STA to study the thermal behavior, and the hyphenated gas analysis system (FTIR and GC-MS) for the characterization of evolved gases during the thermal analysis.

However, we will first discuss the important aspects of this technique, the pitfalls and the troubleshooting we encounter to ensure, from a user perspective, the successful implementation of the method.

Our research has shown that a lead time, ie time elapsed between opening of the cell and the STA/evolved gas analysis (including all preparations), has a pronounced effect on DSC curve of the materials. This is likely to be related to electrolyte

evaporation and unwanted side reactions taking place at the surface of the fully charged anode, which is highly reactive, in the presence of trace amounts of oxygen and/or water[72,73]. An example of such effect is given in **Figure 12**, where DSC curves for graphite electrode with lead time of 4 h, 2 days, and 4 days are compared. The DSC profile of the 4-day lead time anode shows significantly smaller exothermic signals, while the curves for 4 h and 2 days long lead times are very similar.

The assembly of a hand-made full Li-ion battery cell with a thin separator and electrode discs of equal diameters is a delicate operation. Therefore, proper assembly and closure of the cell is of utmost importance for successful electrochemical cycling of the cell and hence, for preparation of electrodes for STA/GC-MS/FTIR characterization. For example, electrode disks' misalignment and/or crimped separator can result in significant changes in the cycling behavior of a full Li-ion cell[74]. Whether the cell is properly assembled, closed, and connected to the cycler can be seen from voltage vs time profile. **Figure 13** shows a number of cycling profiles for faulty cells and compares those to the first cycle of the properly prepared cell. Therefore, we consider all the steps in the cell preparation as critical.

In the note following step 1.2.1 and the paragraph 2 (Calculation of electrode disc's capacity) in the protocol section, it has been mentioned that proper balancing of the electrode disc's areal capacity is an essential requirement prior to full Li-ion battery cell assembling. Therefore, this aspect is of critical importance to avoid overcharging of graphite and Li plating[75,76,77]. **Figure 14** compares DSC curves of fully charged and overcharged graphite, clearly showing a substantial effect of overcharging on the thermal behavior of the material. The overcharged graphite is related to imbalanced electrodes assembly where the cathode's theoretical areal capacity (provided by the supplier: 3.54 mAh/cm^2) is higher than the anode's one (provided by the supplier: 2.24 mAh/cm^2). As a consequence, the graphite becomes overlithiated and the surplus of Li^+ transported to the graphite matrix can be deposited on the surface as Li metal.

Before launching the experimental campaign, preliminary tests were carried out. The technique has been optimized to troubleshoot problems in order to achieve reliable and reproducible results. For example, the choice of a correct plunger for EL-CELL electrochemical cell is essential to avoid bending of the separator. The proper plunger height depends on the materials and thickness of cell components[78]. For the system described in this study, we came to the conclusion that the plunger 50 is of a better choice than plunger 150. Therefore, plunger 50 was consistently used in our experiments.

Similarly, the optimal amount of electrolyte needed to be carefully tuned to ensure good wetting of all cell components. This is necessary to avoid ion transport limitations to a maximum degree possible. Not enough electrolyte results in an increase of ohmic resistance and a loss of capacity[79,80]. The optimized quantity of electrolyte was found to be 150 µL for the system presented in this study.

As for the limitations of the proposed method, some of them are already discussed in the introduction section of the paper. In addition, regarding the mass spectrometry, the decomposition products are typically analyzed using electron ionisation (EI) with quadrupole MS after chromatographic separation by GC. This makes it possible to identify each compound within a complex mixture of evolved gaseous products. However, the chosen settings of the STA/GC-MS limits the detection to small decomposition products with masses below m/z = 150 (The m refers to the molecular

or atomic mass number and z to the charge number of the ion). Nevertheless, the selected parameters for the STA/GC-MS system are deemed appropriate by the authors for the analysis of released gases coming from electrode materials.

Another potential drawback would be a partial condensation of high boiling point products such as ethylene carbonate in the transfer line (heated at 150 °C). As a consequence, careful purging of the entire systems after each experiment is of importance to avoid cross-contamination of experiments.

With respect to FTIR, the evolved gases are transferred through a heated line at 150 °C to a heated TG-IR measurement cell at 200 °C. The analysis of functional groups appearing in the evolved gases enables the identification of gaseous species. A possible disadvantage of the STA/FTIR coupling is the overlapping signals from the gaseous mixture (several gases evolving at the same time) that results in a complex spectra difficult to interpret. In particular, to the contrary of the STA/GC-MS system, there is no separation of decomposition products prior to the infrared absorbance analysis.

The current setup of the gas analysis system allows identification of gaseous compounds, which means the method is qualitative. Indeed, the quantification was not addressed in this study, which leaves potential for additional chemical information to be harvested. This, however, would require the instruments to be connected in series and not in parallel, ie STA/GC-MS and STA/FTIR, to maximize sensitivity and accuracy. In addition, a system for trapping gases after STA analysis would enable the use of GC-MS for quantification after FTIR qualitative characterization. One could consider the following system: STA/trapped gases/ FTIR/GC-MS connected in series. Another consideration is that FTIR could also be used for quantification and cross-validation of quantitative data obtained from GC-MS. The quantification prospect would require anyway further research to determine its applicability in these hyphenated techniques, which was not the scope of our work.

While the present work is qualitative, it offers an improvement on previous work since, as mentioned in the introduction part, the STA equipment is located inside a glovebox, which guarantees the handling of components in a protective atmosphere. Again, to the best of the authors' knowledge, there is limited research published on the thermal behavior of electrode materials, using the exact combination of these analytical instruments STA/FTIR/GC-MS, analytical parameters and sample preparation/handling to elucidate chemical reaction mechanisms at materials level during thermal decomposition. Further details about the significance of this method are provided in the introduction section.

Our research has demonstrated the power of this hyphenated STA/GC-MS/FTIR technique for thermal characterization of battery materials and the analysis of evolved gases. Obviously, this technique can be applied to different set of materials, for example, to study novel materials, materials properties under extreme cycling conditions, etc. This technique is ultimately suitable to investigate thermal behavior of materials and their thermal decomposition routes and to analyses evolving gases. Another example of such use of this hyphenated STA/GC-MS/FTIR technique is the application to characterization of energetic materials, including explosives, propellants and pyrotechnics[81].

Thermal decomposition of lithiated graphite

At low temperature, below 100 °C, an endothermic peak was detected around 70 °C without related mass loss. As mentioned earlier, this peak is as well visible in the pristine graphite anode in contact with electrolyte. The maximum peak

temperature does not correspond to EC melting (ca 36 °C) nor DMC evaporation (90 °C). Some possible explanations include $LiPF_6$-EC melting or HF evolution from $LiPF_6$ salt generated by trace amounts of moisture[82]. However, this endothermic event is not relevant for the purpose of this study since it is not correlated to lithiated graphite. Hence, it was neglected from further analysis.

Region 2 starts with a small CO_2 evolution around 100 °C-110 °C. This is further confirmed with the GC-MS data in **Figure 5** and with the FTIR results displayed in **Figure 4b** that show the presence of CO_2 and H_2O. The solid electrolyte interface (SEI) is a protective layer on the anode surface that grows during the first charge of a cell. It is a result of the electrolyte decomposition upon fresh lithiated graphite. This layer stabilizes the reactive anode surface by preventing further electrolyte decomposition and solvent co-intercalation into graphitic layers in the subsequent charging cycles[83]. It is well known that the less stable components of the SEI layer start to decompose exothermically with an onset temperature around 100 °C-130 °C[35,41,61,84,85]. This phenomenon is often identified as primary SEI decomposition (pSEI). This is consistent with the broad exothermic peak that appears above 100 °C. Interestingly, there is no ethylene evolution detected by FTIR or GC-MS, contrary to expectation from reactions 3, 4, and 9 in **Table 1**. Indeed, the SEI breakdown and subsequent reaction of Li with electrolyte is supposed to take place during this exothermic step, according to the previously mentioned reactions. Moreover, the mass loss in this temperature range is only ca 4 wt%, which is quite low and does not match the expected mass loss from the proposed mechanisms. This mass variation more likely results from the onset of EC evaporation that starts around 150 °C, as depicted by FTIR characteristic 1,863 cm^{-1} absorption peak in **Figure 4a** and **Figure 4c**.

These observations indicate that the SEI layer does not decompose in a single step, as specified in reactions 3, 4, and 9. Therefore, these reactions do not reflect accurately the thermal processes in region 2. Alternatively, reactions 1, 2, and 5 from **Table 1** may provide a better representation of the decomposition reactions as elaborated in the following 100 °C-220 °C range. It is worth mentioning that the CO_2 evolution close to 100 °C could be generated from reaction 2 when traces of water evaporate. It is also possible that, as the temperature increases, the SEI does not disintegrate but its structure and composition modifies, with possible growth of the layer thickness. The mild heat generation, absence of significant mass loss, and evolved gas suggest that reaction 2 in **Table 1** may have induced a change from an insulating SEI structure to a porous one that allows EC interaction or Li-ion transport with the lithiated graphite surface. However, this new or transformed film, called secondary SEI, keeps its protective nature, as evidenced by the low quantity of heat release compared to region 3. It has been found, by means of XRD, that the content of lithium in graphite decreased gradually during thermal ramping from 110 °C to 250 °C, suggesting Li consumption in this temperature interval[86]. When considering the reactants involved in reaction mechanism 1 and 5 (**Table 1**), thermal decomposition 5 is most straightforward and has been selected to describe the process in region 2. The following small endothermic peak around 200 °C can be attributed to the melting of $LiPF_6$, or Li plating[77,87], or graphite exfoliation[88]. This transition event has negligible impact on TR and has therefore been discarded from further analysis and consideration in calculating thermal triplets.

In region 3 (240 °C-290 °C), the increment of the generated heat with an obvious increase of mass loss with the corresponding gas evolution denote a severe phase transition. Based on the thermal analysis results combined with the nature of the gaseous species, multiple consecutive and parallel/or concurrent reaction pathways generate, most probably, peak II. With regards to EC evolution (**Figure 4a** and **Figure 4c**), the STA results from pristine graphite in contact with electrolyte suggest that EC evaporation is faster than EC thermal decomposition under these conditions (measured but not shown). GC-MS data exhibit the presence of PF_3 and ethylene in **Figure 6** and **Figure 7**, respectively, in addition to CO_2 and EC evolution detected by FTIR (**Figure 4a**). Therefore, the following reaction pathways are probably taking place at the same time: a) partial decomposition of secondary SEI, b) Li-electrolyte reactions (reactions 3, 4, 6, 7, 8, and 9 in **Table 1**), c) EC decomposition (reaction 20, **Table 3**), $LiPF_6$ decomposition (reaction 17, **Table 3**) and EC evaporation (**Table 3**). When comparing the exotherm profile obtained for region 2 and region 3, it is very clear that the thermal events occurring in each region are of different nature. This is contradicting the single reaction mechanism reported by some studies[33,35,41] that comprise SEI breakdown and lithiated graphite-electrolyte reactions, as highlighted by reactions 3 and 4. Moreover, the knowledge gained from our results suggests this is not a single thermal event but rather a two-step process. The decomposition mechanisms detailed in reactions 6, 8, and 9 describe better the thermal event in region 3, which is corroborated by the gaseous detection of CO_2, ethylene, and PF_3 (decomposition products of $LiPF_6$). PF_3 is not listed as a primary product of any reactions in **Table 1** and **Table 3** but may be generated in the GC column or heated lines. PF_3 was not generated elsewhere because the thermal decomposition onset of $LiPF_6$ (as shown in reaction 17, **Table 3**) is expected to take place between 100 °C and 200 °C, depending on the experimental conditions (i.e., sealed or open containers, sample size)[89]. One of the products from this thermal decomposition (namely PF5) undergoes a subsequent transformation leading to the formation of POF_3, as shown in reaction 6.

The mass loss in region 3 is mainly due to EC evaporation. Based on these observations, regions 2 and 3 should be modeled differently. We therefore propose and formulate a double breakdown mechanism where the primary SEI does not decompose fully, but changes its structure and composition with simultaneous formation of a secondary SEI layer. As the temperature increases, a second breakdown occurs where the secondary SEI layer decomposes, allowing the consumption of intercalated lithium in the anode.

In region 4, small and partially overlapped peaks are correlated to several decomposition reactions. The analysis of gas evolution with GC-MS displays traces of ethylene in **Figure 7** together with C_2H_6 in **Figure 8**, CH_4 (measured, but not shown), and C_3H_6 (measured, but not shown) only detectable at 15 °C/min. Separate thermal analysis of pristine binder (measured, but not shown) demonstrated that carboxymethyl cellulose (CMC) decomposes over this temperature range. In Reference[90], evidence of specific reactivity of the CMC binder with electrolyte has been reported. This is most probably stemming from the hydroxyl functional groups in CMC (reaction 12, **Table 1**). This process allows the formation of the species that constitute part of the SEI layer. The latter may decompose with a higher heat of reaction than the binder alone may. However, the binder represents only 2 wt% of the anode material, which alone cannot cause the observed heat release. Another explanation would be the subsequent decomposition of more stable products formed in the previous regions during thermal

ramp. Furthermore, it has been revealed that, at 330 °C and 430 °C, exothermic reactions occur because of lithium alkyl carbonate and lithium oxalate decomposition[43]. These components are two of the main SEI species. Since the EC has completely evaporated/decomposed here, the only possible reactions are the ones depicted in 6, 7, 11, and 12 from **Table 1**. However, these reactions do not explain the gases evolved in region 4. It is worth pointing out that the exothermic processes corresponding to this temperature range are different compared to regions 2 and 3, as evidenced by the produced gases, minimal mass loss, the shape of the peak, and the evolved heat. Nevertheless, the decomposition products generated in the previous thermal events, as well as their amounts, may affect reactions in region 4.

Thermal decomposition of NMC (111) cathode

Similar to the DSC patterns obtained in the anode at low temperature, an endothermic peak around 70 °C in region 1 was observed in **Figure 10**, although somewhat less pronounced in this case. CO_2 evolution slightly above 100 °C was equally detected. Both phenomena may be due to an identical mechanism, based on the observations in the anode thermal decomposition patterns. Therefore, this peak was neglected from further consideration.

As mentioned previously, the endotherm around 200 °C (more visible at 15 °C/min in **Figure 11**) in region 2 is due to EC evaporation. This peak overlaps with exothermic thermal events, which makes it difficult to analyze it using the Kissinger method. However, this endothermic event was not discarded and instead, a different approach was applied in this work. Indeed, as mentioned earlier in the representative results section of the cathode, DTG plots at different heating rate were used instead, in order to calculate kinetic parameters with the Kissinger method, for EC evaporation.

In region 3, **Figure 10** indicates an abrupt exothermic peak with sharp CO_2 release and a drop of EC evolution between 240 °C and 290 °C. The possible reactions to describe the gas evolution, mass loss and heat release could be: a) reaction 15 in **Table 2** with HF from decomposed $LiPF_6$ with NMC, b) reaction 19 and 20 for EC reaction with $LiPF_6$ (PF_5) and EC thermal decomposition, respectively, c) EC combustion with released O_2 from NMC decomposition[91] (reaction 16 and reaction 13, respectively), d) autocatalytic NMC decomposition, similar to the one reported for LCO decomposition[33,35,41].

Reaction 15 yields water that was not detected by the gas analysis system. Moreover, this reaction does not contribute to CO_2 emission. Therefore, this reaction is not considered as a relevant process in region 3. Options b) and c) are difficult to distinguish and for this reason, they are both considered for further calculation. The governing reaction is identified in a subsequent stage, when optimizing the simulated thermal response in this temperature interval. A better simulated heat flow signal is obtained when the thermal parameters of EC combustion and evaporation are included in the calculation (not shown in this paper). In a previous DSC study, the thermal curve of NMC(111) did not exhibit a sharp exotherm at 250 °C-290 °C[92]. Interestingly, when EC combustion is excluded from the calculation, the sharp exothermic peak disappears in the simulation and is consistent with the above-mentioned study. The absence of the sharp peak may be related to the use of manually pierced crucibles used in Reference[92] that would allow faster EC evaporation and O_2 release due to a larger opening in the lid. Hence, the sharp exothermic peak is related to EC

combustion (reaction 16, **Table 3**) with released O_2 originated from NMC decomposition (reaction 13, **Table 2**).

Region 4 indicates three exothermic peaks marked I-III. As the temperature reaches 300 °C, more oxygen is produced due to accelerated NMC decomposition. This thermal process is related to the release of physically absorbed oxygen[91]. The CO_2 release observed by FTIR in **Figure 10** is likely the result of conducting carbon additive reaction with oxygen released from delithiated cathode electrode (reaction 14, **Table 2**). This reaction slows down above 350 °C, as the physically absorbed oxygen is being depleted. The temperature range of the second exothermic reaction is in good agreement with PVDF binder decomposition that occurs between 400 °C-500 °C, as observed from DSC measurement of pure NMC binder (measured but not shown). The TGA results show weight losses between 2.97 and 3.54 wt%, which match the expected weight loss associated with PVDF decomposition. The next exothermic process underlying Peak III is correlated to the release of oxygen that is chemically bound in the cathode[91]. This oxygen reacts further with conducting carbon additive to form CO_2 (reaction 14, **Table 2**).

General overview

This work highlights a special combination of experimental features and sample handling in order to collect information about the thermal processes in LIBs' electrodes. Since the equipment is housed inside an argon-filled glove box, the handlings involved from the electrochemical cell assembly to sample preparation and loading in the STA instrument were executed without unintentional contamination of the samples. As a result, an improved accuracy in the determination of thermal parameters could be reached. The electrode was kept unwashed, to better understand the thermal phenomena at material level leading to heat generation and, therefore, potentially contributing to TR. The choice of a crucible with a laser-pierced lid, containing a small hole of 5 µm diameter only, ensures a semi-open system, with results similar to the ones obtained in a sealed crucible, but with the advantage of enabling gas collection.

Moreover, the small size of the hole may potentially reflect the cell phenomena better with its thermally induced reactions, involving gaseous components which are not released instantly, but lead to internal pressure build-up inside the battery cell. This phenomenon, along with uncontrollable increase of cell temperature, may lead to a TR and venting. Another special feature is the broad temperature range, from 5 °C and 600 °C, used in the thermal characterization of electrode materials by STA/FTIR/GC-MS coupled technique.

From these special experimental features and parameters cited above, the most relevant thermal processes were identified and their kinetic thermal triplets could be determined and used to simulate the heat flow signal for each electrode.

To summarize, a double breakdown mechanism is proposed to reflect the decomposition reactions taking place in the anode. The data obtained from STA, FTIR, and GC-MS showed that the primary SEI layer does not decompose fully in a single step. Indeed, there is a simultaneous buildup of a secondary SEI layer. These reactions are modeled with diffusion type decomposition and formation kinetics. At a later stage upon heating, a second breakdown occurs with secondary SEI decomposition and the consumption of Li stored in graphite, EC evaporation, and EC decomposition occurring at the same time. The third exothermic process involves the decomposition of stable products formed in the previous regions and the binder.

The thermal processes identified for NMC (111) cathode decomposition consist of: evaporation of EC, decomposition of NMC with liberation of oxygen, combustion of EC with the liberated oxygen, decomposition of the binder, and combustion of the carbon additive. The evolved O_2 reacts immediately with the carbon additives. Furthermore, EC decomposition does not occur since EC evaporation is faster.

Disclosures

The authors have nothing to disclose.

Acknowledgments

Authors gracefully thank Marc Steen and Natalia Lebedeva for the excellent support reviewing and discussing this manuscript.

References

1. van Ruijven, B. J., De Cian, E., Sue Wing, I. Amplification of future energy demand growth due to climate change. *Nature Communications.* **10**, 2762 (2019).
2. De Cian, E., Sue Wing, I. Global energy consumption in a warming climate. *Environmental and Resource Economics.* **72**, 365-410 (2019).
3. Sivaram, V., Dabiri, J. O., Hart, D. M. The need for continued innovation in solar, wind, and energy storage. *Joule.* **2**, 1639-1642 (2018).
4. Rosewater, D., Williams, A. Analyzing system safety in lithium-ion grid energy storage. *Journal of Power Sources.* **300**, 460-471 (2015).
5. Ferreira, S., Lamb, J., Orendorff, C., Hewson, J., Chalamala, B. *Fundamental Aspects of Large-Scale Energy Storage SystemSafety.* at <https://www.osti.gov/servlets/purl/1365118> (2016).
6. Zhong, G. et al. Thermal runaway and fire behavior investigation of lithium ion batteries using modified cone calorimeter. *Journal of Thermal Analysis and Calorimetry.* **135**, 2879-2889 (2019).
7. Chen, M., Yuen, R., Wang, J. An experimental study about the effect of arrangement on the fire behaviors of lithium-ion batteries. *Journal of Thermal Analysis and Calorimetry.* **129**, 181-188 (2017).
8. Bubbico, R., Greco, V., Menale, C. Hazardous scenarios identification for Li-ion secondary batteries. *Safety Science.* **108**, 72-88 (2018).
9. Ouyang, D. et al. A review on the thermal hazards of the lithium-ion battery and the corresponding countermeasures. *Applied Sciences.* **9**, 2483 (2019).
10. Christman, J. The case of the burning laptops. *Journal of Case Studies.* **30**, 88-97 (2012).
11. US National Transportation Safety Board. Boeing 787 Battery Fire. *Accident No: DCA13IA037.* at <https://www.ntsb.gov/investigations/pages/boeing_787.aspx> (2013).
12. Japan Transport Safety Board & Japan Transport Safety Board. *Aircraft serious incident investigation report. all Nippon Airways Co. Ltd. JA804A.* at <https://www.mlit.go.jp/jtsb/eng-air_report/JA804A.pdf> (2014).
13. Loveridge, M. J. et al. Looking deeper into the galaxy (Note 7). *Batteries.* **4** (2018).
14. Ruiz, V. et al. A review of international abuse testing standards and regulations for lithium ion batteries in electric and hybrid electric vehicles. *Renewable and Sustainable Energy Reviews.* **81**, 1427-1452 (2018).
15. United Nations, E. and S. C. *United Nations Global technical Regulation on Electrical vehicle Safety*

(UN GTR-EVS) on electric vehicle safety: Phase 1. International Organization. **ECE/TRANS/** (2017).

16. International Organization for Standardization. *ISO 6469-1:2019 Electrically propelled road vehicles - Safety specifications - Part 1: rechargeable energy storage system (RESS).* at <https://www.iso.org/standard/68665.html> (2019).
17. Underwriters Laboratories. *Underwriters Laboratories Inc. UL Standard for Safety for Lithium Batteries, UL 1642:2007.* at <https://standardscatalog.ul.com/ProductDetail.aspx?productId=UL1642> (2007).
18. Walker, W. Q., Ali, O. A., Theriot, D. H. in *Future Lithium-ion Batteries.* The Royal Society of Chemistry. 290-315 (2019).
19. Ziebert C, Melcher A, Lei B, Zhao W, R., & M, H. J. S. *Chapter Six - Electrochemical-Thermal Characterization and Thermal Modeling for Batteries. In: Rodriguez-Martinez LM, Omar N, editors. Emerging Nanotechnologies in Rechargeable Energy Storage Systems.* (2017).
20. Ruiz Ruiz, V., Pfrang, A. *JRC Exploratory Research: Safer Li-ion Batteries by Preventing Thermal Propagation.* (2018).
21. Lopez, C. F., Jeevarajan, J. A., Mukherjee, P. P. Experimental analysis of thermal runaway and propagation in lithium-ion battery modules. *Journal of The Electrochemical Society.* **162**, A1905-A1915 (2015).
22. Xiang, H. F. et al. Thermal stability of LiPF6-based electrolyte and effect of contact with various delithiated cathodes of Li-ion batteries. *Journal of Power Sources.* **191**, 575-581 (2009).
23. Juarez-Robles, D., Vyas, A. A., Fear, C., Jeevarajan, J. A., Mukherjee, P. P. Overdischarge and aging analytics of li-ion cells. *Journal of The Electrochemical Society.* **167**, 90558 (2020).
24. Juarez-Robles, D., Vyas, A. A., Fear, C., Jeevarajan, J. A., Mukherjee, P. P. Overcharge and aging analytics of li-ion cells. *Journal of The Electrochemical Society.* **167**, 90547 (2020).
25. Ruiz, V., Brett, L., Steen, M., Van Den Berghe, L. *Putting Science into Standards - Driving Towards Decarbonisation of Transport: Safety, Performance, Second Life and Recycling of Automotive Batteries for e-Vehicles.* (2016).
26. Xiong, R., Ma, S., Li, H., Sun, F., Li, J. Toward a safer battery management system: A critical review on diagnosis and prognosis of battery short circuit. *iScience.* **23**, 101010 (2020).
27. Börger, A., Mertens, J., Wenzl, H. Thermal runaway and thermal runaway propagation in batteries: What do we talk about? *Journal of Energy Storage.* **24**, 100649 (2019).
28. United Nations, E. and S. C. *United Nations Global technical Regulation for Electrical vehicle Safety (UN GTR-EVS): Authorization to develop Phase 2.* at <https://unece-modl.dotsoft.gr/DAM/trans/doc/2017/wp29other/ECE-TRANS-WP29-AC3-49e.pdf> (2018).
29. Zhao, W., Luo, G., Wang, C.-Y. Modeling nail penetration process in large-format li-ion cells. *Journal of The Electrochemical Society.* **162**, A207-A217 (2015).

30. Ren, D. et al. An electrochemical-thermal coupled overcharge-to-thermal-runaway model for lithium ion battery. *Journal of Power Sources.* **364**, 328-340 (2017).

31. Lopez, C. F., Jeevarajan, J. A., Mukherjee, P. P. Characterization of lithium-ion battery thermal abuse behavior using experimental and computational analysis. *Journal of The Electrochemical Society.* **162**, A2163-A2173 (2015).

32. Parmananda, M., Ryali, B., Mukherjee, P. P. Thermo-electrochemical stability analytics of electrode materials. *The Journal of Physical Chemistry C.* **123**, 30106-30120 (2019).

33. Richard, M. N., Dahn, J. R. Accelerating rate calorimetry study on the thermal stability of lithium intercalated graphite in electrolyte. II. Modeling the results and predicting differential scanning calorimeter curves. *Journal of the Electrochemical Society.* **146**, 2078-2084 (1999).

34. Richard, M. N., Dahn, J. R. Accelerating rate calorimetry study on the thermal stability of lithium intercalated graphite in electrolyte. I. Experimental. *Journal of the Electrochemical Society.* **146**, 2068-2077 (1999).

35. Hatchard, T. D., MacNeil, D. D., Basu, A., Dahn, J. R. Thermal model of cylindrical and prismatic lithium-ion cells. *Journal of The Electrochemical Society.* **148**, A755 (2001).

36. Kim, G.-H., Pesaran, A., Spotnitz, R. A three-dimensional thermal abuse model for lithium-ion cells. *Journal of Power Sources.* **170**, 476-489 (2007).

37. Coman, P. T., Rayman, S., White, R. E. A lumped model of venting during thermal runaway in a cylindrical Lithium Cobalt Oxide lithium-ion cell. *Journal of Power Sources.* **307**, 56-62 (2016).

38. Duemichen, E., Braun, U., Senz, R., Fabian, G., Sturm, H. Assessment of a new method for the analysis of decomposition gases of polymers by a combining thermogravimetric solid-phase extraction and thermal desorption gas chromatography mass spectrometry. *Journal of Chromatography A.* **1354**, 117-128 (2014).

39. Yang, H., Shen, X.-D. Dynamic TGA-FTIR studies on the thermal stability of lithium/graphite with electrolyte in lithium-ion cell. *Journal of Power Sources.* **167**, 515-519 (2007).

40. Golubkov, A. W. et al. Thermal-runaway experiments on consumer Li-ion batteries with metal-oxide and olivin-type cathodes. *RSC Advances.* **4**, 3633-3642 (2014).

41. Spotnitz, R., Franklin, J. Abuse behavior of high-power, lithium-ion cells. *Journal of Power Sources.* **113**, 81-100 (2003).

42. Wang, Q., Sun, J., Yao, X., Chen, C. Thermal behavior of lithiated graphite with electrolyte in lithium-ion batteries. *Journal of the Electrochemical Society.* **153**, A329-A333 (2006).

43. Zhao, L., Watanabe, I., Doi, T., Okada, S., Yamaki, J. TG-MS analysis of solid electrolyte interphase (SEI) on graphite negative-electrode in lithium-ion batteries. *Journal of Power Sources.* **161**, 1275-1280 (2006).

44. Choi, N.-S., Profatilova, I. A., Kim, S.-S., Song, E.-H. Thermal reactions of lithiated graphite anode in LiPF6-based electrolyte. *Thermochimica Acta.* **480**, 10-14 (2008).

45. Wang, Q., Sun, J., Yao, X., Chen, C. Thermal stability of LiPF6/EC+DEC electrolyte with charged electrodes for

lithium ion batteries. *Thermochimica Acta.* **437**, 12-16 (2005).

46. Parimalam, B. S., MacIntosh, A. D., Kadam, R., Lucht, B. L. Decomposition Reactions of Anode Solid Electrolyte Interphase (SEI) Components with LiPF6. *The Journal of Physical Chemistry C.* **121**, 22733-22738 (2017).
47. Jakab, E., Mészáros, E., Borsa, J. Effect of slight chemical modification on the pyrolysis behavior of cellulose fibers. *Journal of Analytical and Applied Pyrolysis.* **87**, 117-123 (2010).
48. Kriston, A., Adanouj, I., Ruiz, V., Pfrang, A. Quantification and simulation of thermal decomposition reactions of Li-ion battery materials by simultaneous thermal analysis coupled with gas analysis. *Journal of Power Sources.* **435**, 226774 (2019).
49. Jung, R., Metzger, M., Maglia, F., Stinner, C., Gasteiger, H. A. Oxygen release and its effect on the cycling stability of LiNixMnyCozO2 (NMC) cathode materials for li-ion batteries. *Journal of the Electrochemical Society.* **164**, A1361-A1377 (2017).
50. Buchberger, I. et al. Aging analysis of Graphite/ LiNi1/3Mn1/3Co1/3O2Cells using XRD, PGAA, and AC impedance. *Journal of The Electrochemical Society.* **162**, A2737-A2746 (2015).
51. Wang, Q. S., Sun, J. H., Chu, G. Q., Yao, X. L., Chen, C. H. Effect of LiPF6 on the thermal behaviors of four organic solvents for lithium ion batteries. *Journal of Thermal Analysis and Calorimetry.* **89**, 245-250 (2007).
52. Yang, H., Zhuang, G. V., Ross, P. N. Thermal stability of LiPF6 salt and Li-ion battery electrolytes containing LiPF6. *Journal of Power Sources.* **161**, 573-579 (2006).
53. Campion, C. L., Li, W., Lucht, B. L. Thermal decomposition of LiPF 6-based electrolytes for lithium-ion batteries. *Journal of the Electrochemical Society.* **152**, A2327-A2334 (2005).
54. Zheng, S., Wang, L., Feng, X., He, X. Probing the heat sources during thermal runaway process by thermal analysis of different battery chemistries. *Journal of Power Sources.* **378**, 527-536 (2018).
55. Ren, D. et al. Model-based thermal runaway prediction of lithium-ion batteries from kinetics analysis of cell components. *Applied Energy.* **228**, 633-644 (2018).
56. Chen, Z. et al. Electrochemical degradation mechanism and thermal behaviors of the stored LiNi0.5Co0.2Mn0.3O2 cathode materials. *ACS Applied Materials & Interfaces.* **10**, 25454-25464 (2018).
57. Yu, H.-Y., Zhang, D., Zhu, Z., Lu, Q. Thermal reactivity study of spinel lithium titanium oxide material for lithium ion battery by thermal and spectral analysis. *Journal of Power Sources.* **257**, 96-101 (2014).
58. Zhuang, G. V., Ross, P. N. Analysis of the chemical composition of the passive film on li-ion battery anodes using attentuated total reflection infrared spectroscopy. *Electrochemical and Solid-State Letters.* **6**, A136 (2003).
59. Shurtz, R. C., Engerer, J. D., Hewson, J. C. Predicting high-temperature decomposition of lithiated graphite: Part II. Passivation layer evolution and the role of surface area. *Journal of The Electrochemical Society.* **165**, A3891-A3902 (2018).
60. Mao, B., Huang, P., Chen, H., Wang, Q., Sun, J. Self-heating reaction and thermal runaway criticality of the lithium ion battery. *International Journal of Heat and Mass Transfer.* **149**, 119178 (2020).

61. Watanabe, I., Yamaki, J. Thermalgravimetry-mass spectrometry studies on the thermal stability of graphite anodes with electrolyte in lithium-ion battery. *Journal of Power Sources.* **153**, 402-404 (2006).

62. Fernandes, Y., Bry, A., de Persis, S. Identification and quantification of gases emitted during abuse tests by overcharge of a commercial Li-ion battery. *Journal of Power Sources.* **389**, 106-119 (2018).

63. Feng, X. et al. Investigating the thermal runaway mechanisms of lithium-ion batteries based on thermal analysis database. *Applied Energy.* **246**, 53-64 (2019).

64. Kissinger, H. E. Variation of peak temperature with heating rate in differential thermal analysis. *Journal of Research of the National Bureau of Standards.* **57** (4), 2712 (1956).

65. Kissinger, H. E. Reaction kinetics in differential thermal analysis. *Analytical Chemistry.* **29**, 1702-1706 (1957).

66. Kriston, A., Podias, A., Adanouj, I., Pfrang, A. Analysis of the effect of thermal runaway initiation conditions on the severity of thermal runaway-Numerical simulation and machine learning study. *Journal of The Electrochemical Society.* **167**, 90555 (2020).

67. Ruiz Ruiz, V. et al. The effect of charging and discharging lithium iron phosphate-graphite cells at different temperatures on degradation. *Journal of Visualized Editors: JoVE.* e57501 (2018).

68. National Institute of Standards and Technology. *NIST Chemistry Workbook.* (2018).

69. Sun, Y.-Y., Hsieh, T.-Y., Duh, Y.-S., Kao, C.-S. Thermal behaviors of electrolytes in lithium-ion batteries determined by differential scanning calorimeter. *Journal of Thermal Analysis and Calorimetry.* **116**, 1175-1179 (2014).

70. Larsson, F., Anderson, J., Andersson, P., Mellander, B. E. Thermal modelling of cell-to-cell fire propagation and cascading thermal runaway failure effects for lithium-ion battery cells and modules using fire walls. *Journal of the Electrochemical Society.* **163**, A2854-A2865 (2016).

71. Peng, P., Jiang, F. Thermal behavior analyses of stacked prismatic LiCoO2 lithium-ion batteries during oven tests. *International Journal of Heat and Mass Transfer.* **88**, 411-423 (2015).

72. An, S. J. et al. The state of understanding of the lithium-ion-battery graphite solid electrolyte interphase (SEI) and its relationship to formation cycling. *Carbon.* **105**, 52-76 (2016).

73. Malmgren, S. et al. Consequences of air exposure on the lithiated graphite SEI. *Electrochimica Acta.* **105**, 83-91 (2013).

74. Murray, V., Hall, D. S., Dahn, J. R. A guide to full coin cell making for academic researchers. *Journal of The Electrochemical Society.* **166**, A329-A333 (2019).

75. Kasnatscheew, J. et al. A tutorial into practical capacity and mass balancing of lithium ion batteries. *Journal of The Electrochemical Society.* **164**, A2479-A2486 (2017).

76. Mei, W., Jiang, L., Liang, C., Sun, J., Wang, Q. Understanding of Li-plating on graphite electrode: detection, quantification and mechanism revelation. *Energy Storage Materials.* **41**, 209-221 (2021).

77. Waldmann, T., Hogg, B.-I., Wohlfahrt-Mehrens, M. Li plating as unwanted side reaction in commercial Li-ion cells - A review. *Journal of Power Sources.* **384**, 107-124 (2018).

78. EL-Cell GmbH. *PAT-Core: Lower Plunger Configurator.* at <https://el-cell.com/pat-series/the-pat-core-concept/lower-plunger-configurator/> (2021).

79. Günter, F. J., Burgstaller, C., Konwitschny, F., Reinhart, G. Influence of the electrolyte quantity on lithium-ion cells. *Journal of The Electrochemical Society.* **166**, A1709-A1714 (2019).

80. An, S. J. et al. Correlation of electrolyte volume and electrochemical performance in lithium-ion pouch cells with graphite anodes and NMC532 cathodes. *Journal of The Electrochemical Society.* **164**, A1195-A1202 (2017).

81. Benhammada, A., Trache, D. Thermal decomposition of energetic materials using TG-FTIR and TG-MS: a state-of-the-art review. *Applied Spectroscopy Reviews.* **55**, 724-777 (2020).

82. Ryou, M.-H. et al. Effects of lithium salts on thermal stabilities of lithium alkyl carbonates in SEI layer. *Electrochimica Acta.* **83**, 259-263 (2012).

83. Mao, C. et al. Balancing formation time and electrochemical performance of high energy lithium-ion batteries. *Journal of Power Sources.* **402**, 107-115 (2018).

84. Bandhauer, T. M., Garimella, S., Fuller, T. F. A critical review of thermal issues in lithium-ion batteries. *Journal of the Electrochemical Society.* **158**, R1-R25 (2011).

85. Andersson, A. M., Herstedt, M., Bishop, A. G., Edström, K. The influence of lithium salt on the interfacial reactions controlling the thermal stability of graphite anodes. *Electrochimica Acta.* **47**, 1885-1898 (2002).

86. Chen, Z. et al. Multi-scale study of thermal stability of lithiated graphite. *Energy & Environmental Science.* **4**, 4023-4030 (2011).

87. Waldmann, T. et al. Electrochemical, post-mortem, and ARC analysis of li-ion cell safety in second-life applications. *Journal of the Electrochemical Society.* **164**, A3154-A3162 (2017).

88. Haik, O. et al. On the thermal behavior of lithium intercalated graphites. *Journal of the Electrochemical Society.* **158**, A913-A923 (2011).

89. Solchenbach, S., Metzger, M., Egawa, M., Beyer, H., Gasteiger, H. A. Quantification of PF 5 and POF 3 from side reactions of LiPF 6 in li-ion batteries. *Journal of The Electrochemical Society.* **165**, A3022-A3028 (2018).

90. El Ouatani, L. et al. Surface film formation on a carbonaceous electrode: Influence of the binder chemistry. *Journal of Power Sources.* **189**, 72-80 (2009).

91. Li, J., Zhang, Z. R., Guo, X. J., Yang, Y. The studies on structural and thermal properties of delithiated LixNi1/3Co1/3Mn1/3O2 (0<x≤1) as a cathode material in lithium ion batteries. *Solid State Ionics.* **177**, 1509-1516 (2006).

92. Fleischhammer, M., Waldmann, T., Bisle, G., Hogg, B.-I., Wohlfahrt-Mehrens, M. Interaction of cyclic ageing at high-rate and low temperatures and safety in lithium-ion batteries. *Journal of Power Sources.* **274**, 432-439 (2015).